

**School of Mechanical and Manufacturing Engineering**

**Faculty of Engineering**

**The University of New South Wales**

**Internal Condition Monitoring of a  
Planetary Gearbox**

by

**Melinda Paige Blake**

Submitted: November 2015

Student ID: z3417864

Supervisor: Dr. Wade Smith

## **I. Certificate of Originality**

I, Melinda Paige Blake, hereby declare that this submission is my own work and to the best of my knowledge it contains no materials previously published or written by another person, or substantial proportions of material which have been accepted for the award of any other degree or diploma at UNSW or any other educational institution, except where due acknowledgement is made in the thesis. Any contribution made to the research by others, with whom I have worked at UNSW or elsewhere, is explicitly acknowledged in the thesis.

I also declare that the intellectual content of this thesis is the product of my own work, except to the extent that assistance from others in the project's design and conception in style, presentation and linguistic expression is acknowledged.

Signed .....

Date .....

## **II. Abstract**

Planetary gearboxes are common in industry applications requiring high transmission ratios and load-bearing capacities, such as wind turbines and helicopters. The frequent component damage and system failures that result from the difficult operating conditions of such applications are costly in terms of economic losses and human casualties, and as such, the development of effective condition monitoring techniques is of great importance. Vibration machine condition monitoring for fixed-axis gearboxes is well established, however the fundamentally different structure of planetary gearboxes means that fixed-axis methods cannot be directly applied. Several alternatives have been proposed, with the most successful methods relying on time synchronous averaging. The use of internal accelerometers in the vibration monitoring of planetary gearboxes is a more recent development.

The purpose of this project was twofold. Firstly, an attempt to establish the usefulness or otherwise of the internal accelerometer in the detection of gear faults was to be made. Examination of the raw data and some preliminary signal processing showed the internal data to be at least equally clear in showing the presence of faults in the time domain to the external data, but unforeseen processing problems inhibited a full analysis of frequency spectrum data.

Secondly, interference and signal dropout problems with the UNSW planetary gearbox test rig that inhibit the effective use of the internal accelerometer were to be resolved. Various mechanical and processing fixes have been implemented, and were found to be effective.

### **III. Acknowledgements**

With thanks to my supervisor, Dr. Wade Smith, for his advice and assistance over the course of this past year. My thanks also to Karel Ruber for his time and help in installing the NVGate software package.

I would like to extend my appreciation and thanks to the laboratory staff of the Willis Annexe, in particular Vincenzo Carnevale and Stephen Kuhle for their invaluable assistance with the gearbox test rig.

I would also like to acknowledge the use in this thesis of data and code passed on by Andrew Bligh and Tianchao Shao.

Finally, with gratitude, to Munaum.

## IV. Nomenclature

### Symbols

$f_c$  Carrier frequency

$f_{input}$  Input frequency

$f_p$  Absolute planet frequency

$f_{p/c}$  Planet frequency relative to the carrier

$f_s$  Absolute sun frequency

$f_{s/c}$  Sun frequency relative to the carrier

$n$  Number of planet gears

$N_p$  Number of teeth on the planet gears

$N_{pinion}$  Number of teeth on the pinion gear

$N_r$  Number of teeth on the ring gear

$N_s$  Number of teeth on sun gear

$N_{spur}$  Number of teeth on spur gear

### Abbreviations

**CBM** Condition-based maintenance

**EMC** Electro-magnetic compatibility

**EMI** Electro-magnetic interference

**FFT** Fast Fourier Transform

**FPGMF** Faulty planet gear mesh frequency

**PPF** Planet pass frequency

**RGMF** Ring gear mesh frequency

**SGMF** Spur gear mesh frequency

**TSA** Time synchronous averaging

**UNSW** University of New South Wales

**VFD** Variable-frequency drive

## V. Contents

|  |    |
|--|----|
| Chapter 1 .....  | 1  |
| Introduction.....  | 1  |
| 1.1 The Planetary Gearbox .....                                    | 1  |
| 1.2 Condition Monitoring and Vibration Analysis .....              | 3  |
| 1.3 Project Aims.....  | 5  |
| 1.4 Thesis Structure .....   | 5  |
| Chapter 2.....   | 7  |
| Literature Review.....   | 7  |
| 2.1 Introduction to Vibration Analysis of Planetary Gearboxes..... | 7  |
| 2.2 Time-Synchronous Averaging .....                               | 9  |
| 2.3 The McFadden Method.....                                       | 10 |
| 2.3.1 Howard’s composite signal averaging technique .....          | 11 |
| 2.4 The “Australian Patent” .....                                  | 12 |
| Chapter 3.....   | 17 |
| Experimental Methodology .....                                     | 17 |
| 3.1 The UNSW Test Rig.....   | 17 |
| 3.1.1 The planetary gearbox.....                                   | 19 |
| 3.2 Instrumentation and Data Acquisition .....                     | 21 |
| 3.2.1 The variable-frequency drive .....                           | 21 |
| 3.2.2 The front-end device .....                                   | 22 |
| 3.2.3 The NVGate software package .....                            | 23 |

|  |    |
|--|----|
| 3.3 Operating Conditions and Procedures .....      | 23 |
| 3.3.1 Test settings .....                          | 24 |
| 3.3.2 Operating procedures .....                   | 26 |
| Chapter 4 .....                                    | 28 |
| Results .....                                      | 28 |
| 4.1 Raw Data .....                                 | 28 |
| 4.1.1 Test 2 .....                                 | 30 |
| 4.1.2 Test 4 .....                                 | 34 |
| 4.1.3 Test 8 .....                                 | 37 |
| 4.1.4 Test 12 .....                                | 39 |
| 4.1.5 Some conclusions .....                       | 42 |
| 4.2 The Secondary Aims .....                       | 43 |
| 4.2.1 Electro-magnetic interference .....          | 43 |
| 4.2.2 Random signal dropouts .....                 | 44 |
| 4.2.3 Apparent signal damping .....                | 46 |
| Chapter 5 .....                                    | 47 |
| Signal Processing .....                            | 47 |
| 5.1 Signal Processing Methodology .....            | 47 |
| 5.2 Preliminary Results .....                      | 48 |
| Chapter 6 .....                                    | 53 |
| Conclusion .....                                   | 53 |
| 6.1 Some Conclusions .....                         | 53 |
| 6.2 Future Work .....                              | 55 |
| 6.3 The Future of the Internal Accelerometer ..... | 55 |
| Chapter 7 .....                                    | 57 |
| References .....                                   | 57 |



|   |    |
|---|----|
| Chapter 8.....  | 61 |
| Appendices.....   | 61 |
| Appendix A.....   | 62 |
| A.1 Gear tooth numbers.....                                   | 62 |
| A.2 Gearbox frequency equations.....                          | 63 |
| A.3 Gearmesh frequency equations .....                        | 65 |
| A.4 Significant frequencies.....                              | 66 |
| A.5 Planet tooth mesh count for the ring gear .....           | 68 |
| Appendix B .....  | 70 |
| Appendix C .....  | 71 |
| Appendix D.....   | 72 |
| D.1 Code used to plot the example undamaged gear signal ..... | 72 |
| D.2 Time domain plotter.....                                  | 74 |
| D.3 Logarithmic frequency spectrum plotter .....              | 75 |
| D.4 Frequency difference in faulty signal plotter .....       | 76 |
| D.5 Frequency spectrum comparison plotter .....               | 78 |
| D.6 Smoothing code.....                                       | 80 |
| D.7 Order tracking code.....                                  | 81 |
| D.8 Code to plot order-tracked samples .....                  | 84 |

## VI. List of Figures

|   |           |
|---|-----------|
| <b>Figure 1: The standard layout of a planetary gearbox with three planet gears (Forrester, 1998).</b>                                    | <b>2</b>  |
| <b>Figure 2: A single-stage planetary gearbox found in the main rotor of the Oryx helicopter (de Smidt, 2009).</b>                        | <b>3</b>  |
| <b>Figure 3: The effect of complex transmission paths on a vibration signal (Randall &amp; Antoni, 2011).</b>                             | <b>8</b>  |
| <b>Figure 4: The rectangular, triangular and Hanning windows in the time domain and frequency spectrum (McFadden, 1994)</b>               | <b>11</b> |
| <b>Figure 5: Comparison of the "Australian patent" and McFadden methods for a seeded planet gear fault (Forrester &amp; Blunt, 2003).</b> | <b>13</b> |
| <b>Figure 6: Vibration transmission paths for external and internal accelerometers (Hilbert et al., 2013).</b>                            | <b>14</b> |
| <b>Figure 7: Internal time signals (1) raw, (2) cepstrum whitened, and (3) MED filtered (Fan &amp; Li, 2015).</b>                         | <b>15</b> |
| <b>Figure 8: Layout of the UNSW large gearbox test rig (Bligh, 2012).</b>   | <b>17</b> |
| <b>Figure 9: The UNSW test rig gearbox, illustrating the parallel stage and the slip ring.</b>  | <b>18</b> |
| <b>Figure 10: Schematic of the parallel and planetary stages (from Bligh, 2012).</b>  | <b>19</b> |
| <b>Figure 11: (1) The half root crack, (2) the quarter root crack, and (3) the spall.</b>   | <b>21</b> |
| <b>Figure 12: The control panel of the UNSW test rig. The FRENIC-MEGA VFD is located on the left.</b>                                     | <b>22</b> |
| <b>Figure 13: The OR35 integrated analyser and the "UNSW MK II Transducer Indicator".</b>   | <b>23</b> |

|  |           |
|--|-----------|
| <b>Figure 14: The complete internal time domain signal for Test 2. ....</b>  | <b>30</b> |
| <b>Figure 15: A segment of the internal time domain signal for Test 2. ....</b>  | <b>31</b> |
| <b>Figure 16: Complete internal frequency spectrum for Test 2 showing RGMF. ....</b>   | <b>31</b> |
| <b>Figure 17: A segment of the internal frequency spectrum for Test 2. ....</b>  | <b>32</b> |
| <b>Figure 18: The complete external time domain signal for Test 2. ....</b>  | <b>32</b> |
| <b>Figure 19: A segment of the internal time domain signal for Test 2. ....</b>  | <b>33</b> |
| <b>Figure 20: Complete external frequency spectrum for Test 2 showing SGMF. ....</b>   | <b>33</b> |
| <b>Figure 21: A segment of the external frequency spectrum for Test 2. ....</b>  | <b>34</b> |
| <b>Figure 22: A segment of the internal time domain signal for Test 4. ....</b>  | <b>35</b> |
| <b>Figure 23: The difference in the internal frequency spectrum in Test 4 from the baseline. ....</b>  | <b>35</b> |
| <b>Figure 24: A segment of the external time domain signal of Test 4. ....</b>   | <b>36</b> |
| <b>Figure 25: The difference in the external frequency spectrum in Test 4 from the baseline. ....</b>  | <b>36</b> |
| <b>Figure 26: A segment of the internal time domain signal for Test 8. The arrows indicate a number of fault impacts. ....</b>                 | <b>37</b> |
| <b>Figure 27: A segment of the external time domain signal for Test 8. ....</b>  | <b>38</b> |
| <b>Figure 28: The residual internal frequency spectrum of Test 8 and the baseline signal. ....</b>   | <b>38</b> |
| <b>Figure 29: The residual external frequency spectrum of Test 8 and the baseline signal. ....</b>   | <b>39</b> |
| <b>Figure 30: A segment of the internal time signal for Test 12. ....</b>  | <b>40</b> |
| <b>Figure 31: A segment of the external time signal for Test 12. ....</b>  | <b>40</b> |
| <b>Figure 32: The internal frequency spectrum for Test 12 (blue) and the baseline (orange). ....</b>   | <b>41</b> |
| <b>Figure 33: The external frequency spectrum for Test 12 (blue) and the baseline (orange). ....</b>   | <b>41</b> |
| <b>Figure 34: Power spectral density of an internal vibration signal recorded prior to modifications to cabling (Fan &amp; Li, 2015). ....</b> | <b>43</b> |

|  |    |
|--|----|
| <b>Figure 35: Random signal drop-outs in the frequency spectrum.</b> .....   | 45 |
| <b>Figure 36: Unsmoothed time signal (blue) and smoothed time signal (orange).</b> .....                           | 45 |
| <b>Figure 37: External order-tracked data for Test 2. The x-axis is in shaft revolutions.</b> ...                  | 49 |
| <b>Figure 38: External order-tracked frequency data for Test 2. Note that the x-axis is in shaft orders.</b> ..... | 49 |
| <b>Figure 39: Internal order-tracked data for Test 2.</b> .....  | 50 |
| <b>Figure 40: Internal frequency data for Test 2.</b> .....  | 50 |
| <b>Figure 41: Comparison of external order-tracked data for Test 4 (blue) and the baseline (orange).</b> .....     | 51 |
| <b>Figure 42: Comparison of internal order-tracked data for Test 4 (blue) and the baseline (orange).</b> .....     | 51 |
| <b>Figure 43: FFT of the tachometer signal for Test 1.</b> .....   | 66 |

## VII. List of Tables

|   |    |
|---|----|
| <b>Table 1: Specifics of instrumentation and data acquisition devices.</b>                          | 21 |
| <b>Table 2: Test data.</b>  | 24 |
| <b>Table 3: Kurtosis values for all tests.</b>  | 29 |
| <b>Table 4: Gear tooth numbers.</b>   | 62 |
| <b>Table 5: Average input frequencies.</b>  | 66 |
| <b>Table 6: Significant frequencies.</b>  | 67 |
| <b>Table 7: Tooth mesh count between a planet gear and the ring gear.</b>                           | 68 |
| <b>Table 8: Specifications of the Brüel &amp; Kjær 4394 accelerometer (Brüel &amp; Kjær, 2015).</b> | 70 |
| <b>Table 9: Summary of test operating conditions.</b>   | 71 |

# Chapter 1

## Introduction

In Chapter 1 following is given an overview of the history, structure and use of the planetary gearbox. Condition-based monitoring with an emphasis on vibration analysis techniques for planetary gearboxes is briefly discussed. The project aims are set out. An outline of the thesis structure is provided.

### 1.1 The Planetary Gearbox

The epicyclic gearbox was first conceived of in 1781 by James Watt, in a sun-and-planet configuration for use in the emerging steam engine technology (Princeton, 2010). The planetary gearbox is a type of epicyclic gearbox commonly found in industry applications requiring a compact and light-weight solution to high loads and large transmission ratios, most notably in heavy automobiles, wind turbines, helicopter transmissions, and winch and lifting applications (Fan & Li, 2015; Lei et al., 2014).

There are four main components in the planetary gearbox: the annulus (or ring) gear, the sun gear, the planet gears, and the planet carrier. A planetary gearbox will generally include three or more planet gears, although fewer may be used in rare cases. **Figure 1** following illustrates the standard layout for a planetary gearbox with three planet gears.

In a standard planetary gearbox, the sun gear and planet carrier act as input and output, with the annulus gear being fixed. In the planetary gearbox investigated here, the planet carrier is the input and the sun gear the output. As the planet gears rotate around the sun gear, in addition to rotating around their own axes, planetary gearboxes are known as unfixed-axis (Lei et al., 2014). While it is theoretically possible to fix the planet carrier instead of the annulus

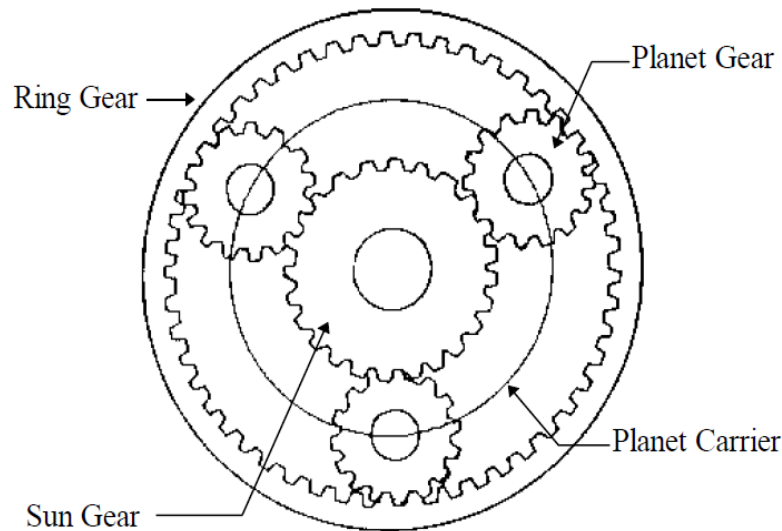


**Figure 1: The standard layout of a planetary gearbox with three planet gears (Forrester, 1998).**

gear, thus creating a fixed-axis planetary gearbox, such a system has few practical uses and is not commonly found in industrial applications. As such this arrangement will not be here discussed further.

The primary advantage of the planetary gearbox is that large speed and torque ratios may be generated by a relatively compact system. Further, as the input and output shafts are in-line, unlike in parallel arrangements equipment is able to be mounted along the same central axis (Bligh, 2012). Another advantage over the parallel arrangement is the low noise characteristics of the planetary gearbox.

These advantages of the planetary gearbox, particularly the high load-bearing capacity and high transmission ratio mean it is ideally suited to use in heavy-duty industrial applications such as wind turbines and helicopters, as shown in **Figure 2** following. However, planetary gearboxes in these applications operate under difficult working conditions, which results in a high failure rate of critical gear and bearing components (Fan & Li, 2015; Lei et al., 2014). As subsequent system failures risk significant economic losses and human casualties – 1 in 145 wind turbines suffer a gearbox failure each year at a cost of \$200,000 - the ability to predict component failure through effective machine condition monitoring is of great importance (Frith, 2015).



**Figure 2: A single-stage planetary gearbox found in the main rotor of the Oryx helicopter (de Smidt, 2009).**

## **1.2 Condition Monitoring and Vibration Analysis**

Common maintenance strategies prior to the introduction of condition-based maintenance (CBM) were run-to-break and time-based preventative, resulting in either catastrophic failure or excessive maintenance and part replacement. CBM has obvious advantages over the earlier maintenance strategies, allowing as it does for operational run-time to be maximized while the risk of catastrophic failure is minimized (Randall, 2011). However, the frequent or continuous condition monitoring required for CBM to be effective is difficult to implement in many industries, meaning it is usually found in applications where both catastrophic failure and machine downtime are extremely costly (Bligh, 2012). The wind turbine industry is a prime example of such an application, with gearbox failure costing the industry in excess of US\$250 million per year (Frith, 2015).

There are two primary machine condition monitoring techniques: lubricant analysis and vibration analysis. Lubricant analysis involves taking oil samples from sealed gearboxes and investigating the particles contained therein; in industrial applications it is generally more costly and difficult to implement than the alternative (de Smidt, 2009).

In comparison to lubricant analysis, vibration analysis has several advantages. Equipment for recording and analysis is less expensive, and installation of systems is generally simpler. As ambient vibration is low in most contexts, contamination by environmental factors is not a major concern. It is also possible to take a reference vibration signal from the machine



before installation or shortly afterwards, against which later vibration signals may be compared (Lyon, 1987).

As such vibration machine condition monitoring is the more common technique, relying on the vibration signals generated by periodic events such as, in the case of the planetary gearbox, shaft rotation and gear tooth meshes. Changes in the frequency spectrum of the vibrations indicate changes to the condition of the machine, and as such vibration monitoring can be used to detect part faults and predict system failure (Randall, 2011; Bligh, 2012). It is commonly applied in gearbox monitoring to the detection of gear and bearing faults, and techniques for the vibration analysis of parallel gearbox arrangements are sophisticated.

In the vibration monitoring of planetary gearboxes, accelerometers are usually located externally on the fixed annulus gear. Although this positioning minimizes difficulties with installation, maintenance and data collection, the complex transmission structure complicates the vibration signal, and as such vibration-based condition monitoring for planetary gearboxes is underdeveloped in comparison with fixed-axis systems (Bligh, 2012). Nevertheless, a number of vibration-based fault diagnosis methods for planetary gearboxes have been proposed, falling approximately into four categories: the time-domain methods, the frequency-domain methods, the time-frequency-domain methods, and a small number of other methods (Lei et al., 2014).

Time-domain methods are generally the simplest and easiest to implement of these, and the most successful is the McFadden method. This makes use of the well-established time synchronous averaging (TSA) technique to extract the vibration signal of individual gear teeth through windowing, and thus reconstruct the complete vibration signal of the gear of interest (McFadden, 1991; McFadden, 1994). The “Australian patent” was a later proposal. Again a time-domain method, it attempts to overcome issues associated with the windowing in the TSA method by instead using a selective time filtered signal averaging technique. However, this method has not been met with widespread acceptance (Forrester, 1998; Forrester & Blunt, 2003).

The use of internal accelerometers in vibration machine condition monitoring for planetary gearboxes is a relatively recent development. This new technique attempts to avoid the distortion of vibration signals in data obtained from external accelerometers due to the complex transmission structure by locating the accelerometer internally, on the planet carrier. Data are extracted via a slip-ring or wireless transmission.

Initial results pertaining to the use of the internal accelerometer in planet gear and bearing diagnostics are promising, although only three independent implementations of the technique are known to date: at the University of Pretoria, using a slip-ring configuration; at the University of New South Wales, using the slip-ring configuration; and the i-Mass implementation in Europe, using wireless transmission (de Smidt, 2009; Bligh, 2012; Hilbert et al., 2013).

### **1.3 Project Aims**

The primary aim of this project is to establish the usefulness, or otherwise, of internal accelerometers in the vibration-based gear fault detection of planetary gearboxes. Although there are a number of existing publications on the use of the internal accelerometer in relation to rolling-element bearing faults, concerning its use in planet gear diagnostics there is only one prior work (Fan & Li, 2015; de Smidt, 2009). This project hopes to validate the conclusions of that work.

The secondary aim of the project is to address a number of problems associated with the implementation of the internal accelerometer in the UNSW large gearbox test rig. Previous internal vibration data was subject to electro-magnetic interference (EMI) and random signal dropout problems that inhibited the effective analysis of the data. The EMI was believed to originate in some way from the variable frequency drive (VFD). The cause of the random signal dropouts was not known, but was believed to be independent of the EMI. The secondary aim is to address these problems at their source, or to develop methods to overcome the effects of these problems during signal analysis. This outcome of this investigation is addressed in **Chapter 4**.

Finally, during the first round of testing it was noticed that the internal accelerometer was generating a highly unusual signal, and impact testing suggested that the signal was being heavily damped for unknown reasons. The outcome of the investigation into this issue is also addressed in **Chapter 4**.

### **1.4 Thesis Structure**

Chapter 1: Introduction to the planetary gearbox. Brief background to condition monitoring and vibration analysis with emphasis on epicyclic methods. Overview of the aims of the project.

Chapter 2: Overview of existing literature on vibration monitoring methods used for planetary gearboxes. Particular emphasis is placed on the relatively new internal accelerometer technique.

Chapter 3: Description of the UNSW large gearbox test rig and associated controls and data acquisition devices. Overview of test conditions. Correct operating procedures for the test rig are given.

Chapter 4: Preliminary results of the 14 tests prior to signal processing and analysis. A comprehensive overview of the investigation and outcomes of the secondary project aims is given.

Chapter 5: Signal processing and analysis methods. Some conclusions in regards to individual samples.

Chapter 6: Conclusions to the primary project aim. A comprehensive listing of potential improvements to the methodology is given. The future of the internal accelerometer technique is addressed.

Chapter 7: List of references.

Chapter 8: Refer to Appendices for a full description.

## Chapter 2

### Literature Review

In Chapter 2 following is given an overview of existing methods for the vibration analysis of planetary gearboxes. Time-synchronous averaging is discussed. Particular emphasis is placed on the more common time-domain methods, particularly the McFadden and “Australia patent” methods. A comprehensive review of the existing literature on the use of the internal accelerometer in planetary gearboxes is given.

Vibration machine condition monitoring is a well-established field. For the sake of brevity, the current state of literature on condition-based maintenance (CBM) and the field of vibration monitoring in general is not explored in greater detail than that given in Chapter 1 above, and this review is focused instead on the applications of vibration-based fault diagnosis to gear systems, and planetary gearboxes in particular.

#### 2.1 Introduction to Vibration Analysis of Planetary Gearboxes

Publications on the vibration machine condition monitoring of planetary gearboxes are relatively few in relation to those concerning fixed-axis gearboxes, although there has been a noticeable growth in recent years. This disparity is due to certain problems associated with the complex gear transmission structure of planetary gearboxes that prevent the use of standard fixed-axis methods (Lei et al., 2014).

Lei et al. propose a breakdown of these problems into four distinct behaviours. The primary difficulty of planetary gearbox vibration analysis is the complexity and variability of the vibration transmission paths from the gearmesh points to externally-located accelerometers, as shown in **Figure 3** following. The other problematic behaviours are:

- The simultaneous meshing of multiple planet gears, generating similar vibrations that may neutralize each other.
- The appearance of asymmetric sidebands in the frequency spectra of non-faulty gearboxes, as a result of the different meshing phases of the planet gears.
- The masking of vibration characteristics of low-speed components by heavy noise (Lei et al., 2014).

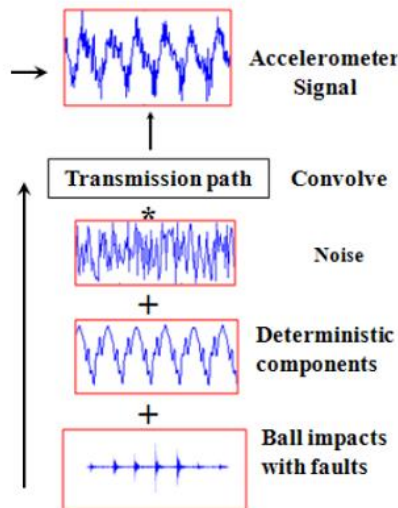


**Figure 3: The effect of complex transmission paths on a vibration signal (Randall & Antoni, 2011).**

The majority of publications regarding the vibration machine condition monitoring of planetary gearboxes are reliant on signal post-processing, and methods may be classed under one of four approximate categories (Lei et al., 2014):

1. Time-domain methods, including the statistical indicators method of Wu et al., McFadden's time synchronous averaging, and Forrester's time filtered signal averaging (Wu et al., 2004; McFadden, 1991; Forrester, 1998)
2. Frequency-domain methods that depend for the most part on the Fourier transform.
3. Time-frequency-domain methods that make use of the Wigner–Ville distribution and wavelet transforms. These methods are generally more effective than time-domain and frequency-domain methods but are more complex.
4. A number of other methods that cannot be classed as time-domain, frequency-domain, or time–frequency-domain. These methods make use of advanced signal

processing techniques such as spectral kurtosis, cyclostationary analysis and stochastic resonance.

Of these categories, time-domain methods are the most widely used, being significantly less complex and more direct than those of the other categories (Lei et al., 2014). Many of these time-domain methods make use of time-synchronous averaging (TSA), an overview of which is presented below.

## 2.2 Time-Synchronous Averaging

The TSA method was first proposed as a tool in fixed-gear fault diagnostics in the 1970's, when Stewart developed a number of powerful diagnostic tools that now serve as the benchmark for helicopter gearbox diagnostics (Stewart, 1977). It was not until 1985 that McFadden first attempted to adapt the method to planetary gearbox systems (McFadden & Smith, 1985). The primary function of TSA when applied to gear fault diagnostics in planetary gearboxes is to extract the vibration signal of the gear of interest from the overall vibration signal of the gearbox, by averaging a number of signal segments in order that the deterministic component becomes dominant (Randall, 2011; Bligh, 2009).

In a practical sense, TSA is carried out by averaging a number  $N$  of signal segments taken from a vibration signal  $y(t)$ , that are in length equal to one period  $T$  of the synchronising tachometer signal, or to the percentage of that period corresponding to the period of the gear of interest. Mathematically this is expressed as:

$$y(t) = \frac{1}{N} \sum_{n=0}^{N-1} y(t + nT)$$

This is modelled as the convolution of  $y(t)$  with a series of  $N$  delta functions with a spacing  $T$ , which creates a comb filter passing the periodic frequency harmonics. The filter passes fewer non-harmonic components for higher  $N$ , but this is limited practically to that achievable in a reasonable signal sampling time. Such a method readily allows for the extraction of the gear signal of interest from a fixed-axis gearbox. However, complications associated with the unique vibration characteristics of planetary gearbox systems require heavy modification of TSA methods to allow for their application to planetary gearboxes, and the presence of multiple similar planet gears in such gearboxes poses a significant problem to the method.

It should be noted that order tracking is almost always applied before TSA methods are used, and as such ‘time’ in fact corresponds to rotation angle. The method is nevertheless still described as time synchronous averaging if nominally constant speeds are considered. Further, TSA is generally applied to systems with nominally constant loads, as there are additional complexities associated with varying load cases (Randall, 2011).

### **2.3 The McFadden Method**

The first attempt at a TSA method for planetary gear diagnostics was presented by McFadden in 1985 (McFadden & Smith, 1985). This method attempted to obtain signal averages for individual planets and the sun gear using a single external accelerometer, in order that standard signal averaging techniques could be directly applied to the resulting signal for the purpose of gear fault diagnostics. This was followed by a comb filter model for extracting periodic waveforms through the use of time domain averaging – a method applicable to gear diagnostics, though it was not exclusively intended for such a use (McFadden, 1986). This comb filter model was flawed, and later a revision was issued that instead made use of a rectangular window in the time domain and Fourier transform signal sampling in the frequency domain (McFadden, 1987).

The McFadden windowing technique that now dominates vibration-based gear fault diagnostics for planetary gearboxes was first proposed in 1991. The windowing technique relies on the fact that for an accelerometer mounted externally on the annulus gear or housing, the dominant contribution to the composite vibration signal is made by the planet gear in closest proximity to the accelerometer. Thus, as the planet passes the accelerometer, the signal may be sampled over a short period, or ‘window’. The sampling window must be of adequate length to capture the complete vibration signal of one tooth, but short enough that the relative motion of the accelerometer and planet gear does not dramatically modulate the vibration signal (McFadden, 1991).

Assuming a hunting-tooth design, on the next pass of that planet a different tooth will be in mesh with the annulus gear, and based upon standard kinematics it is a simple matter to determine the tooth mesh sequence if gear tooth numbers are known (Randall, 2011). Given the lack of signal modulation resulting from relative motion over such a short period, the TSA of each window is easily determined. The signal post-processed tooth window can thus be easily mapped into position in the time domain of the gear. A number of gear fault diagnostic

methods may then be applied. This method with minor modifications may also be applied to determine the TSA of the sun gear (McFadden, 1991).

McFadden based the choice of sampling window on two conditions, that the minimum window size is no less than that of a single tooth, and that the window shape when mapped must sum to unity (de Smidt, 2009). The original McFadden windowing method made use of a non-overlapping rectangular sampling window (McFadden, 1991). This resulted in discontinuities at window boundaries than manifested themselves as noise in the amplitude spectrum and errors in the time domain average.

A revised method was issued that allowed for the use of certain alternative window functions, specifically the triangular and Hanning windows which both sum to unity when mapped. It was determined that the use of a triangular or Hanning sampling window completely eliminated noise components resulting from the vibration of the other planets, and also that the Hanning window significantly reduced errors occurring at lower frequencies (McFadden, 1994). **Figure 4** below illustrates the rectangular, triangular and Hanning windows in the time domain and frequency spectrum. Use of the Hanning window is now widely accepted (Randall, 2011).

### 2.3.1 Howard's composite signal averaging technique

As part of an investigation into the early detection of gear faults in planetary gearboxes used in helicopter transmissions, Howard conducted a comparison of the McFadden method with a composite signal averaging technique as applied to planet gears and the sun gear (Howard, 1991). It was found that McFadden's TSA method produced superior results to

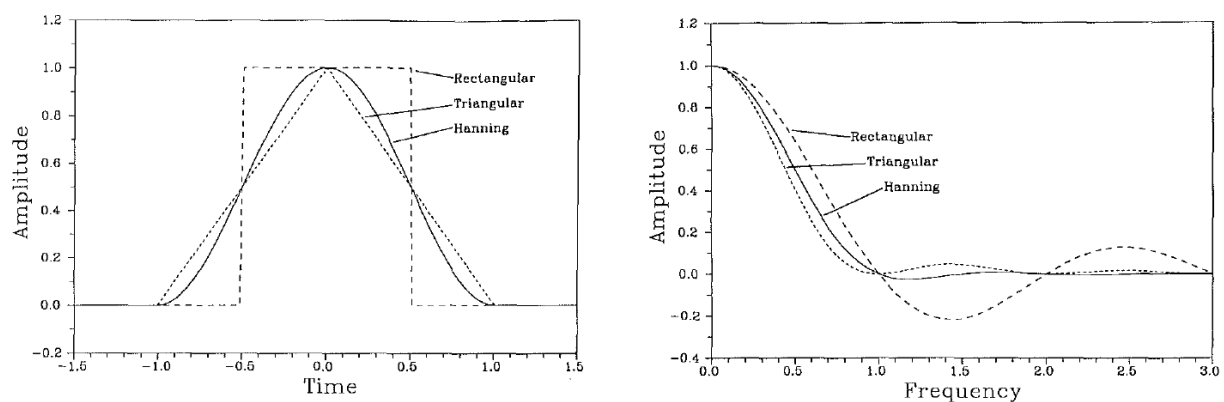


**Figure 4: The rectangular, triangular and Hanning windows in the time domain and frequency spectrum (McFadden, 1994)**



Howard's composite signal averaging technique when used to detect faults in the individual planet gears.

However, the McFadden method was less sensitive to faults in the sun gear than Howard's composite signal averaging technique, assuming an optimal placement of the accelerometer for the detection of sun gear faults through composite averaging. For McFadden's TSA method, Howard recommends a minimum of  $N$  of 20 tooth mesh cycles, regardless of whether the gear of interest is a planet gear or the sun gear.

## **2.4 The “Australian Patent”**

The revised McFadden method was a notable improvement on the original proposal, in terms of the reduction of amplitude spectrum noise and time domain average errors (McFadden, 1994). However, it failed to solve certain issues associated with the practical implementation of the method to vibration machine condition monitoring in industry, namely, the comparatively long time required to obtain a vibration signal of sufficient length for McFadden's TSA method to become effective. It should also be noted that the use of the Hanning window did not completely eliminate errors resulting from discontinuities (Forrester, 1998).

The “Australian patent” method was put forward by Forrester as an alternative to the McFadden method. It is based on the understanding that the total planet gear vibration signal as measured by an externally mounted accelerometer will be the sum of vibrations of the individual planet gears, amplitude modulated by the planet passes. The planet vibrations are separated from the total vibration by use of a selective continuous time filter chosen to minimise noise from other planets. That is to say, the technique makes use of the fact while the dominant component of the signal as recorded by the external accelerometer will be from the nearest planet gear, the other planet gears still contribute. As the TSA is calculated from a continuous sample rather than the discrete windows of the McFadden method, discontinuity errors are avoided (Forrester, 1998).

Two potential selective continuous time filters are proposed, the simpler of which is:

$$b(t) = (1 + \cos(2\pi f_c t))^{P-1}$$

where  $f_c$  is the frequency of the planet carrier and  $P$  is the number of planet gears.

The “Australian patent” method was found to be a significant improvement on the McFadden method, giving an improvement of up to 90% in detection of a single tooth fault

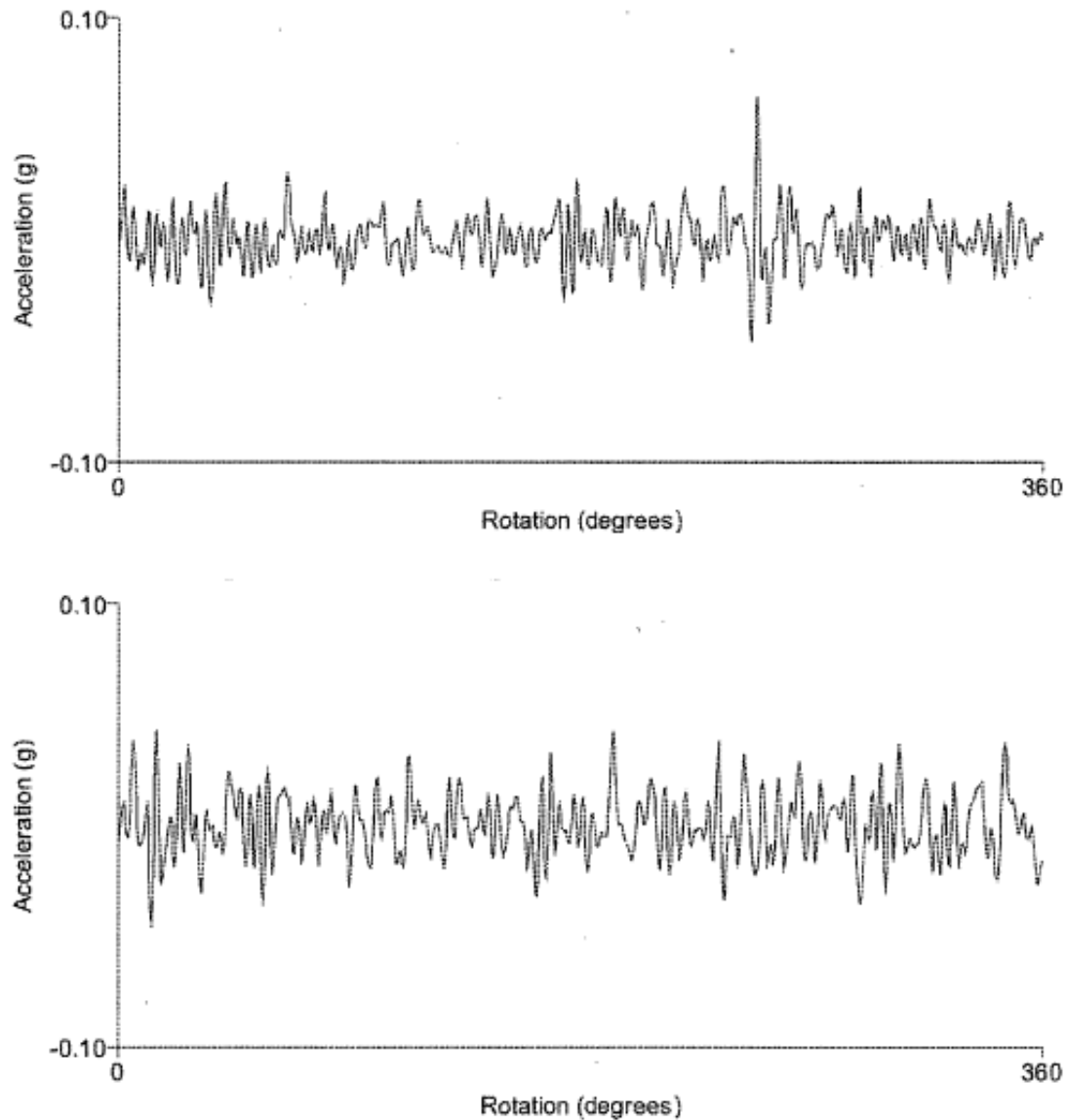


**Figure 5: Comparison of the "Australian patent" and McFadden methods for a seeded planet gear fault (Forrester & Blunt, 2003).**

using the residual kurtosis method (Forrester, 1998). **Figure 5** shows an example comparison of the "Australian patent" and McFadden methods for a seeded planet gear fault, where residual kurtosis produced a value of 3.1 for the McFadden method and a value of 5.9 for the "Australian patent" method.

Forrester also argued that the "Australian patent" method is better suited to industry applications as use of the continuous filter means significantly less sampling time is required for the TSA to be effective. Despite these apparent advantages, the "Australian patent" method

has failed to gain widespread recognition, and as such the McFadden windowing method is still the standard.

## 2.5 The Internal Accelerometer

In comparison with TSA methods for fixed-axis gearboxes, the McFadden method and the “Australian patent” method are more complex and less effective at detecting gear faults, and comparable bearing fault detection methods for planetary gearboxes have been found to be similarly lacking (Forrester & Blunt, 2003). The use of internal accelerometers mounted in the planet carrier is intended to improve the quality of the vibration data extracted by reducing the complexity of the vibration transmission path from the gear to the accelerometer (Hilbert et al., 2013). **Figure 6** below shows the vibration transmission paths for external and internal accelerometers in a planetary gearbox with a fixed annulus gear.

To date there have been three independent implementations of the internal accelerometer technique in planetary gearboxes: at the University of Pretoria, at the University of New South Wales, and the i-MaSS project in Europe (de Smidt, 2009; Bligh, 2012; Hilbert et al., 2013).

de Smidt’s use of the internal accelerometer was the first attempt at internal vibration monitoring of a planetary gearbox. An accelerometer was located internally in the planet carrier of a modified three-planet Bonfiglioli epicyclic gearbox, with vibration signals being

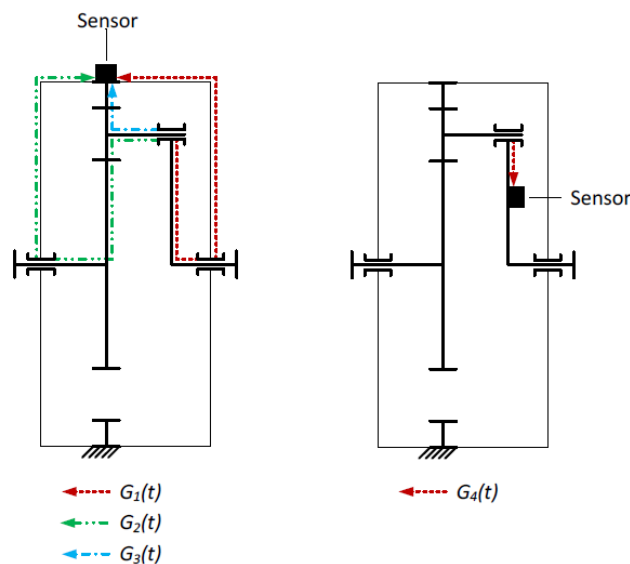


**Figure 6: Vibration transmission paths for external and internal accelerometers (Hilbert et al., 2013).**

transmitted through a slip-ring. Simple condition indicators were used to compare internal vibration data with data obtained from an externally located accelerometer. The external vibration data were processed with standard TSA methods for planetary gearboxes (de Smidt, 2009).

It was found that internal and external vibration data were equally useful in detecting the degradation of the epicyclic gearbox, and in some cases the internal data were more effective in diagnosing damage to planet gears. Internal vibration data also required less complex signal post-processing. However, de Smidt noted that industry applications of the technique will be restricted by the need to make major modifications to the planetary gearbox in order to accommodate the internal accelerometer and slip-ring. de Smidt concluded that internally mounted accelerometers have the potential to be very effective in industrial vibration machine condition monitoring of planetary gearboxes, once wireless technologies have developed to permit a sufficiently high data transmission rate for wireless accelerometers to be useful (de Smidt, 2009).

The second attempt at the development of a planetary gearbox incorporating an internal accelerometer was made by Bligh at UNSW. The gearbox was of a non-hunting-tooth design and also included a second accelerometer located externally on the fixed annulus gear. It was found that neither accelerometer was successful in detecting bearing faults, as both vibration

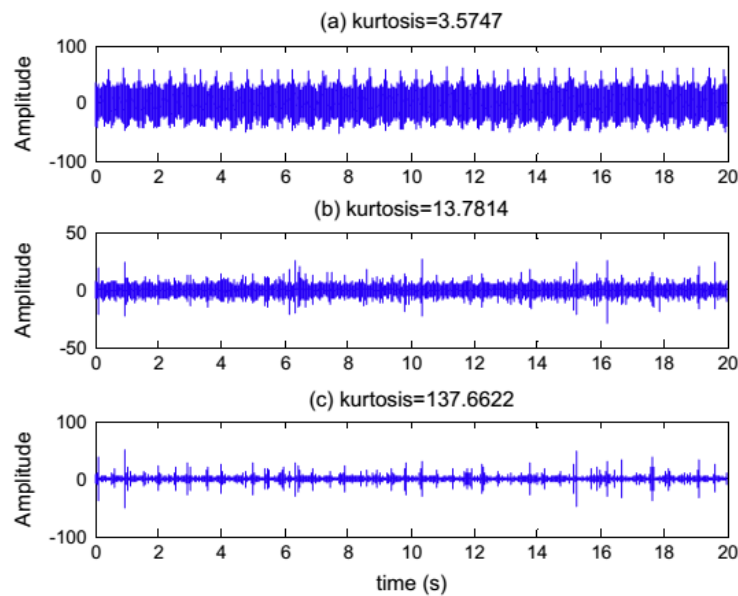


**Figure 7: Internal time signals (1) raw, (2) cepstrum whitened, and (3) MED filtered (Fan & Li, 2015).**

signals were overshadowed by other components (Bligh, 2012). It is this, the UNSW large gearbox test rig, that is investigated in this report.

The later analysis of Fan and Li found that the internal and external vibration data were at least equally useful in detecting outer race faults in rolling-element planet bearings, and that the internal accelerometer was much more effective in detecting faults in the inner race (Fan & Li, 2015). **Figure 7** above illustrates the time signal and related kurtosis values for various signal processing techniques, as measured by the internal accelerometer.

The UNSW planetary gearbox test rig has since been redesigned to accommodate a hunting-tooth design. Although some papers have been published regarding gear faults diagnosis using the internal accelerometer on the original UNSW planetary gearbox design, on that subject there are as yet no publications making use of the new hunting-tooth design (Smith et al., 2013).

Building on the earlier work of de Smidt, the recent paper by Hilbert et al. regarding the i-MaSS project proposed to wirelessly transmit the vibration signal from a standard Low-Voltage ICP/IEPE accelerometer located in the planet carrier of a closed planetary gearbox, for the purpose of monitoring the deterioration of planet bearing condition (Hilbert et al., 2013). This proposal has since been implemented, and although publication is still forthcoming, Hilbert has indicated that preliminary results suggest that the experiment was at least somewhat successful (Hilbert, 2015).

## Chapter 3

# Experimental Methodology

In Chapter 3 following is described the UNSW large gearbox test rig, including the arrangement of the external and internal accelerometers, and the types of gear faults investigated. An overview of the data acquisition system and software is given. Provided below also is an overview of the test conditions, and an outline of the correct procedures for operation of the test rig.

### 3.1 The UNSW Test Rig

The UNSW large gearbox test rig was built by Sweeney in 1996 initially in a parallel configuration for the purpose of verification of a mathematical model of transmission error (Sweeney & Randall, 1996). The test rig was later rebuilt in a non-hunting-tooth planetary configuration, in order to investigate the usefulness of the internal accelerometer in the vibration condition monitoring of rolling element bearings (Bligh, 2012). As a result of more

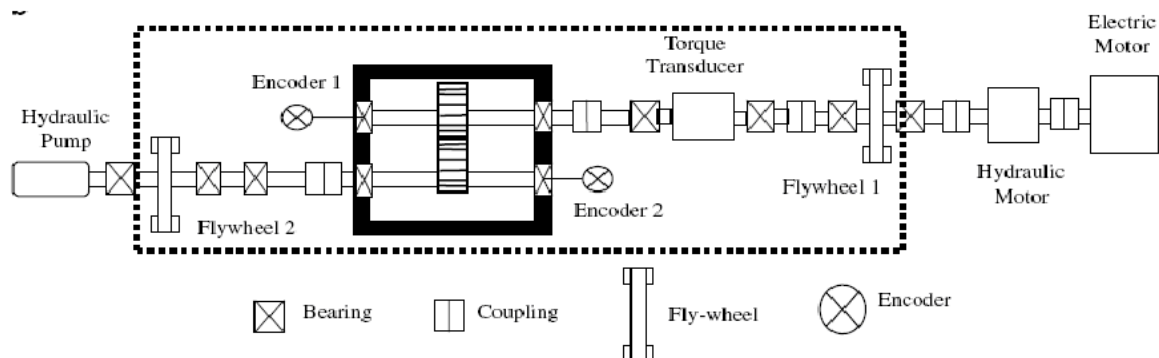


**Figure 8: Layout of the UNSW large gearbox test rig (Bligh, 2012).**

recent modifications, the configuration of the test rig as it currently stands is a hunting-tooth planetary gearbox with a single parallel stage at the input, with integrated internal accelerometer. It is used in the vibration condition monitoring of both rolling element bearings and planetary gears (Fan & Li, 2015; Shao, 2015).

The UNSW large gearbox test rig illustrated in **Figure 8** above is powered primarily by the recirculating hydraulic pump and motor system, with a 3-phase AC induction motor used to overcome the losses. The hydraulic system is also used to generate the torque load, which is measured by an in-line torque transducer located between the AC motor and the gearbox. The system also incorporates two large flywheels, in order to minimize speed fluctuations.

The test rig has two independent systems for applying the hydraulic load: low-load and high-load. In the tests outlined following only the low-load system was used. The gearbox was originally designed to be loaded by the hydraulic system to at least 100 Nm, but due to the implementation of the belt drive system, it is presently restricted to approximately 70 Nm. Torque as measured by the in-line transducer is displayed in real time on the custom-built “UNSW MK II Transducer Indicator”. Due to the great complexity involved in calibrating the in-line torque transducer, it was not recalibrated before testing commenced, and as such all displayed values are approximate.

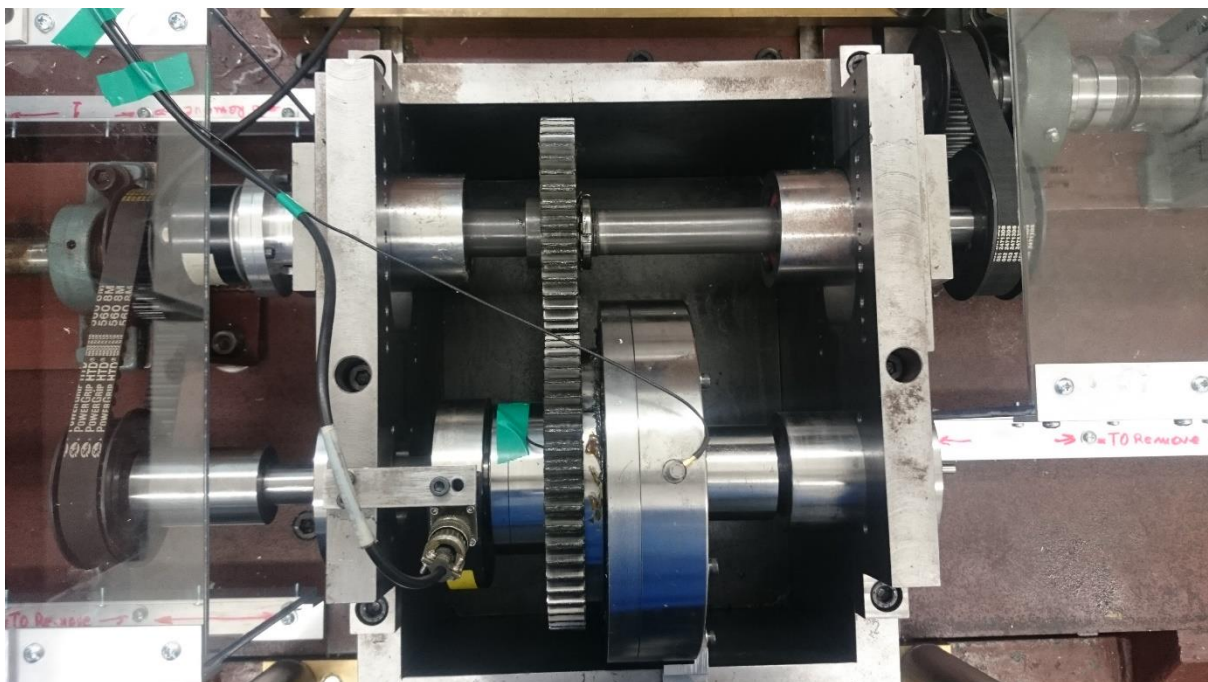


**Figure 9: The UNSW test rig gearbox, illustrating the parallel stage and the slip ring.**

The gearbox interfaces with the test rig structure via a series of flexible couplings and belts, with the housing set on sliding rails to allow for proper belt tensioning, as shown in **Figure 9** above. Mounted to the input shaft (namely, the parallel stage) is a Heidenhain shaft encoder that outputs a once-per-revolution pulse via a Westlands signal conditioner (not shown). A Michigan Scientific slip ring used to transmit the internal accelerometer signal is mounted **concentrically to the output shaft**. Specifics of this equipment are given in **Table 1** in the following section (the torque transducer is omitted as the specifics are not known).

Both the internal and external accelerometers are of the integrated-circuit Brüel & Kjær 4394 type. The external accelerometer is secured by a stud to the top surface of the ring gear casing and transmits its signal directly to the OR35 front-end device. The internal accelerometer is located in a recess in the spur gear, and is bolted to the planet carrier between the spur and ring gears. The signal is transmitted to the OR35 front-end device via the slip ring.

### 3.1.1 The planetary gearbox

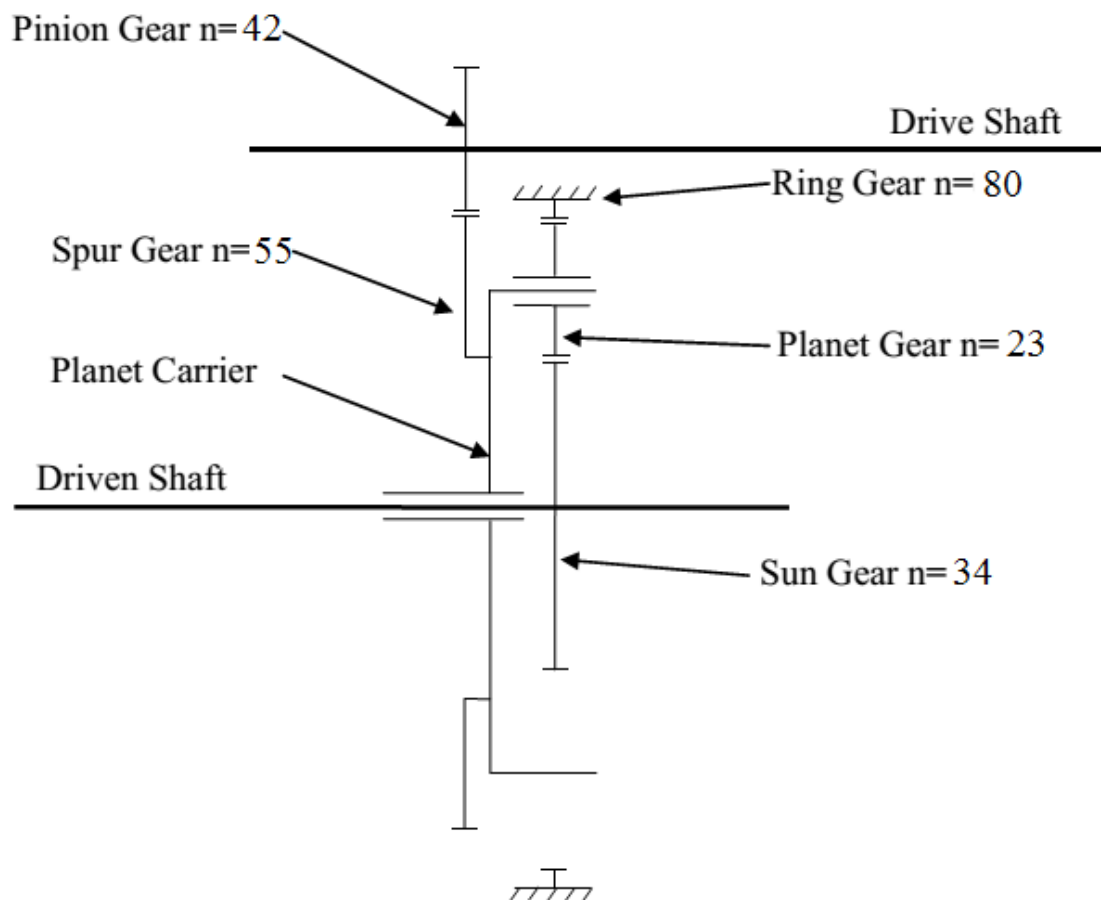


**Figure 10: Schematic of the parallel and planetary stages (from Bligh, 2012).**



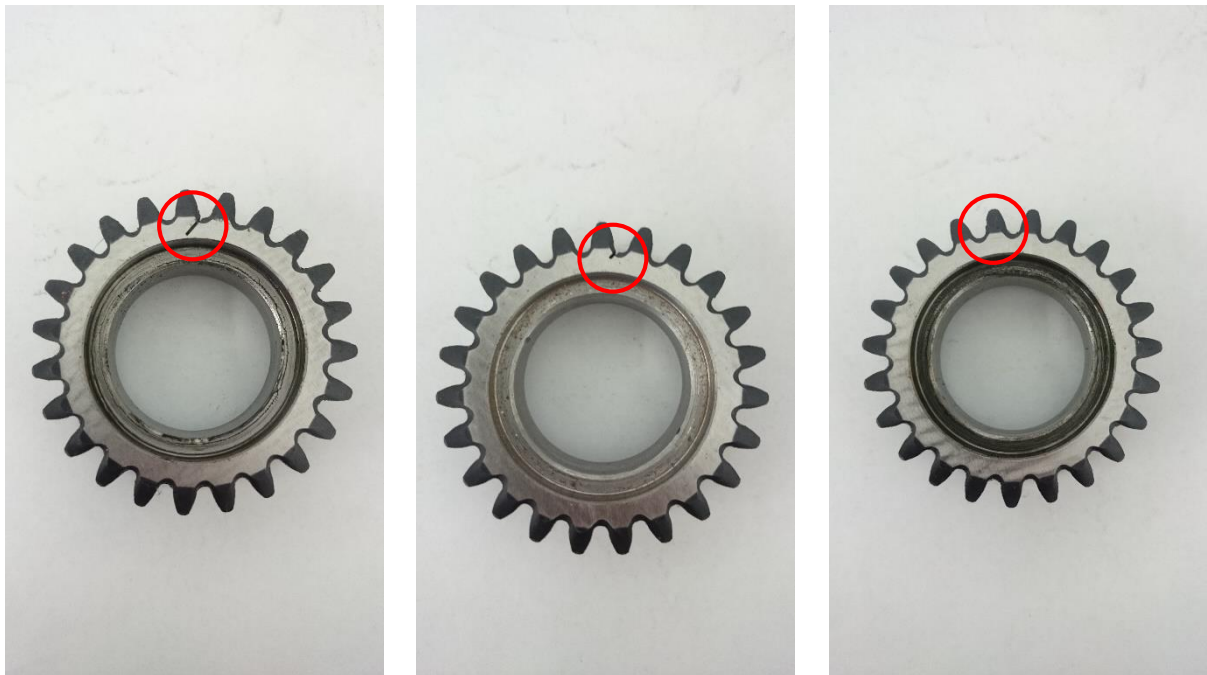
The gearbox interfaces with the test rig structure via a number of belts and flexible couplings, and includes both parallel and planetary stages. The parallel shaft is the driving input and the planetary shaft is the driven output.

As shown in **Figure 10** above, the parallel stage involves a 42-tooth pinion gear on the drive shaft and a 55-tooth spur gear on the driven shaft. It is inside this spur gear, which is rigidly affixed to the planet carrier, that the internal accelerometer is located. The Heidenhain shaft encoder in combination with the signal conditioner provides a once-per-revolution tachometer signal of the pinion drive shaft.

The planetary stage is of a standard configuration, with the planet carrier acting as the input, the 34-tooth sun gear as the output, and the 80-tooth ring gear to which the external accelerometer is mounted being fixed. The planet carrier supports three 23-tooth planet gears, and it is these gears (and the associated bearings) that are interchangeable for the purpose of vibration condition monitoring. These tooth numbers give an overall gear ratio of 1:2.56 (Shao, 2015). The internal accelerometer is mounted to the planet carrier as close as practically possible to the centre of rotation of one planet gear.

A summary of these gear tooth numbers may be found in Table 3 in Appendix A below.

The UNSW test rig is supplied with six of the 23-tooth planet gears. Of these, three are undamaged and three have artificially seeded faults. The types of faults were:



1. Half root crack: a 0.5 mm slot at 45° across half the tooth root width.
2. Quarter root crack: a 0.5 mm slot at 45° across one-quarter of the tooth root width.
3. Spall: a 1 mm wide by 0.25 mm deep slot machined across the pitch point of one tooth.

All three fault types as well as a reference scenario with three undamaged gears were investigated. The types of planet gear damage are illustrated in **Figure 11** above.

### 3.2 Instrumentation and Data Acquisition

There are three primary devices involved in control and data acquisition procedures for the UNSW test rig: the FRENIC-MEGA variable-frequency drive (VFD), the OR35 front-end integrated analyser, and the laptop running the NVGate software. Specifics of the VFD and the integrated analyser, as well as electrical equipment described in the above section, are given in **Table 1** below.

**Table 1: Specifics of instrumentation and data acquisition devices.**

**Figure 11: (1) The half root crack, (2) the quarter root crack, and (3) the spall.**

| Function                               | Manufacturer        | Product No.                        |
|--|---------------------|------------------------------------|
| Accelerometers (internal and external) | Brüel & Kjær        | 4394                               |
| Slip ring                              | Michigan Scientific | B6-2                               |
| Shaft encoder                          | Heidenhain          | ROD 426.0000 - 3600                |
| Signal conditioner                     | Westlands           | S2                                 |
| Torque real-time display               | Custom              | UNSW MK II<br>Transducer Indicator |
| Variable frequency drive               | Fuji Electric       | FRN7.5G1E-4A                       |
| Front-end integrated analyser          | OROS                | OR35                               |

#### 3.2.1 The variable-frequency drive

Shown in **Figure 12** below, the 3-phase AC induction motor is controlled by a FRENIC-MEGA variable frequency drive with a built-in electro-magnetic compatibility (EMC) filter. The VFD allows the AC motor speed to be maintained at a constant nominal



**Figure 12: The control panel of the UNSW test rig. The FRENIC-MEGA VFD is located on the left.**

value, or for a continuously variable signal to be input. As the AC motor is a 4-pole type, the speed given on the display is four times the actual nominal value. In the following tests the display input was 16 Hz, giving a nominal input speed of 4 Hz.

The FRENIC-MEGA VFD also allows for its carrier frequency to be modified. Initially the carrier frequency was set variously to 14 kHz or 16 kHz, and as mentioned above there was observable electro-magnetic interference (EMI) visible in the internal acceleration signal at these frequencies. In the tests outlined in the following section, based upon expert advice the VFD carrier frequency was changed to 2 kHz.

### 3.2.2 The front-end device

Previously the front-end device used with this rig was the Brüel & Kjær PULSE platform and Labshop software (Bligh, 2012). This has since been substituted with OROS' newer OR35 integrated analyser, as shown in **Figure 13** below, and the corresponding NVGate software package.

The OR35 is an 8-channel integrated analyser designed to record and process vibration and noise signals at sampling frequencies of up to 102.4 kHz (OROS, 2015). In the tests outlined below, the internal accelerometer, external accelerometer, and tachometer signals



**Figure 13: The OR35 integrated analyser and the “UNSW MK II Transducer Indicator”.**

correspond to inputs 1, 2, and 3 respectively. A moderate sampling frequency of 25.6 kHz was used, giving a useable frequency range of 12.8 kHz.

### 3.2.3 The NVGate software package

The OR35 communicates with the laptop via an Ethernet cable and USB dongle. A template (termed a “worksheet” in the software) to record the three acceleration and tachometer input signals was created in NVGate. Although the NVGate software package does allow for the generation of real-time frequency spectrum plots, this template only made use of the time-domain “Record” function, displaying the vibration signals in time and acceleration, and the tachometer signal in time and frequency. The “start-to-time” option was used to restrict sample lengths to precisely 300 seconds.

The specifications for the Brüel & Kjær 4394 accelerometers were manually input into the template (refer to Appendix B for specifications). As the tachometer signal was output by a combined shaft encoder and signal conditioner system of unknown type, specifications for this were unknown and default settings were used.

## 3.3 Operating Conditions and Procedures

There were two attempts made to record vibration data from the internal and external accelerometers on the UNSW test rig. Initially ten 300-second samples were recorded,

including all fault types in both orientations and the undamaged reference signal at a torque load of 50 Nm, and two additional samples at 65 Nm. It was then discovered that the internal accelerometer was not generating the expected signal, and a thorough investigation into the cause of the fault was carried out. The fault was diagnosed as a missing section of cable between the accelerometer and the slip ring, possibly a result of the removal of the rig to an offsite location for servicing of the hydraulic system. After the fault was repaired, further testing was conducted.

### 3.3.1 Test settings

In the second round of testing, two sets of seven samples were taken, at torque loads of 50 Nm and 65 Nm respectively. Each set included a reference sample of three undamaged gears, and tests of each gear fault type in both orientations. The fault types and load torques for all fourteen tests are given in **Table 2** below.

In the following table, the ‘/’ and ‘\’ symbols under “Fault Type” refer to the orientation of the half and quarter root cracks, when observed from the right-hand side of the planetary gearbox in **Figure 9** above. ‘L’ and ‘R’ describe the side of the tooth the spall is cut into from the same perspective. Under “Holding Torque” is displayed the torque load for the test rig running at speed with the low-load system fully open. “Load Torque (Start)” is the average torque at the start of the recording. As the torque drops by 1-2 Nm over the duration of the 300-second sample, the displayed torque load at the end of the record is noted under “Load Torque (End)”.

As noted earlier, the in-line torque transducer was not able to be recalibrated before the samples were recorded due to the complexities of the process, and as such all values for torque noted here are approximate.

**Table 2: Test data.**

| Test No. | Fault Type          | Holding Torque | Load Torque (Start) | Load Torque (End) |
|----------|---------------------|----------------|---------------------|-------------------|
| 1        | Undamaged           | 35 Nm          | 50 Nm               | 47 Nm             |
| 2        | Undamaged           | 33 Nm          | 65 Nm               | 64 Nm             |
| 3        | Half root crack (/) | 33 Nm          | 50 Nm               | 49 Nm             |

|           |                        |       |       |       |
|-----------|------------------------|-------|-------|-------|
| <b>4</b>  | Half root crack (/)    | 31 Nm | 65 Nm | 64 Nm |
| <b>5</b>  | Half root crack (\)    | 31 Nm | 50 Nm | 50 Nm |
| <b>6</b>  | Half root crack (\)    | 30 Nm | 65 Nm | 63 Nm |
| <b>7</b>  | Quarter root crack (/) | 31 Nm | 50 Nm | 49 Nm |
| <b>8</b>  | Quarter root crack (/) | 31 Nm | 65 Nm | 63 Nm |
| <b>9</b>  | Quarter root crack (\) | 30 Nm | 50 Nm | 49 Nm |
| <b>10</b> | Quarter root crack (\) | 29 Nm | 65 Nm | 63 Nm |
| <b>11</b> | Spall (L)              | 30 Nm | 50 Nm | 49 Nm |
| <b>12</b> | Spall (L)              | 29 Nm | 65 Nm | 63 Nm |
| <b>13</b> | Spall (R)              | 28 Nm | 50 Nm | 50 Nm |
| <b>14</b> | Spall (R)              | 29 Nm | 65 Nm | 63 Nm |

The nominal running speed of the motor was 4 Hz (due to slip the actual running speeds were on average 3.808 for the 50 Nm load cases and 3.785 for the 65 Nm cases). This speed was thought to be sufficiently great that the vibration data collected would be useful, but not so high that belt slippage would become an issue. This speed was also chosen to match that used in previous tests by Shao, in order to establish that the recent servicing of the hydraulics had not had a significant impact on the vibration characteristics of the test rig (Shao, 2015).

All gears were tested at both 50 Nm and 65 Nm. 50 Nm was selected as the low value as it was a safe margin above the variable holding torque. Although the test rig is intended to run at loads up to 100 Nm, over 70 Nm belt slippage is a major concern, and an high torque load of 65 Nm was preferred for this reason. A third torque load of ~ 80 Nm would be useful however this is not possible with the current configuration of the test rig.



In the first round of testing the sampling frequency was 12.8 kHz, but as this was found to give an insufficiently great useful frequency range it was increased in the second round to 25.6 kHz. A higher sampling frequency would potentially provide more useful information, but as the samples taken are very long, the signal processing time required makes a higher sampling frequency unfeasible. The 300-second sample length was selected to provide a sufficiently meaningful number of averages for signal processing.

A summary of the operating conditions may be found in **Table 9** in Appendix C below.

### 3.3.2 Operating procedures

The procedure for the recording of a single 300-second sample is given here. This procedure omits the checks on safety guards and cable routing made before every test. Note also that due to the difficulty involved in removing the test rig's safety guards, the gears were regreased at every changeover of planet gear rather than before every test. Frequencies given below refer to display frequencies.

1. **Set up:** The torque transducer is connected to the display, the three accelerometer and tachometer inputs to the OR35, and the OR35 to the laptop with the NVGate template running.
2. **Power on:** With the emergency stop engaged, the main power cable is plugged into the 3-phase power outlet and the outlet switched on. The emergency stop is disengaged.
3. **Check hydraulics:** The low-load hydraulic loading system is engaged and set to fully open.
4. **Start up:** The VFD is powered on. In 0.1 Hz increments, the test rig is manually started and speed increased to 2 Hz.
5. **Speed up:** In increments of 1 Hz, the speed is manually increased to the required nominal display frequency of 16 Hz.
6. **Apply load:** Using the low-load system, the hydraulic load is gradually increased to an average value (the hydraulic load is prone to rapid fluctuations up to 2 Nm from the centre value) of 50 Nm or 65 Nm.
7. **Run in:** The rig is allowed to run in for 60 seconds.
8. **Record sample:** Using the “start-to-time” function, a 300-second sample is recorded in NVGate at a sampling frequency of 25.6 kHz.
9. **Remove load:** When the sample is complete, the low-load system is gradually restored to fully open.

10. **Reduce speed:** In increments of 1 Hz the speed is reduced to 2 Hz, and in increments of 0.1 Hz to zero.
11. **Power off:** The VFD is powered off, the emergency stop reengaged, the power at the outlet switched off, and the power cable unplugged.

After each sample is taken, it is saved into the NVGate project. Unlike the PULSE system originally used with the UNSW test rig, samples can be exported as .mat files directly from the NVGate project and thereafter manipulated in Matlab.



## Chapter 4

### Results

In Chapter 4 following is presented a range of time domain and frequency spectrum plots for a representative selection of tests samples. Some preliminary conclusions as to the usefulness of the data are made. A comprehensive overview of the investigation into and outcomes of the secondary project aims is also given here.

#### 4.1 Raw Data

As is comprehensively detailed in **Chapter 3** above, two sets of 7 tests were run covering the full range of fault types and gear orientations. The time domain and frequency spectrum presented below concern a representative selection of these tests. Full data sets for all 14 test samples have been made available to the School of Mechanical and Manufacturing Engineering at UNSW.

Further, note that the plots presented below are derived from the raw data. No signal processing has been carried out on the data, with the exception of that integral to the operation of the OR35 integrated analyser, such as anti-aliasing. The intended purpose of this is to make evident the usefulness of data derived from the internal accelerometer, even in an unprocessed state.

For derivation of input shaft speeds for the 50 Nm and 65 Nm load cases, refer to **Appendix A**. There was a sufficient difference between the two load cases to warrant recalculation of the significant frequencies for each, but between individual tests for each load case the input speed difference was negligible.

Due to problems with apparently highly damped internal signal, discussed in **4.2 The Secondary Aims** below, it was decided that first the kurtosis of the raw internal and external signals should be taken, as a measure of whether the internal signal was behaving as expected. These values are given in **Table 3** below. Note that a kurtosis around 3 indicates minimal impulsive phenomena, and higher kurtosis value such as 11 indicates a high impulsivity (de Lorenzo & Calabro, 2007).

**Table 3: Kurtosis values for all tests.**

| Test No.  | Internal Kurtosis | External Kurtosis |
|-----------|-------------------|-------------------|
| <b>1</b>  | 2.9964            | 3.6064            |
| <b>2</b>  | 3.0001            | 3.8581            |
| <b>3</b>  | 50.2380           | 55.3096           |
| <b>4</b>  | 32.2930           | 44.0813           |
| <b>5</b>  | 15.2344           | 24.9534           |
| <b>6</b>  | 19.5131           | 31.7831           |
| <b>7</b>  | 3.6693            | 4.8473            |
| <b>8</b>  | 3.7889            | 4.6364            |
| <b>9</b>  | 3.1689            | 4.7715            |
| <b>10</b> | 3.2119            | 4.4296            |
| <b>11</b> | 10.9328           | 17.9380           |
| <b>12</b> | 8.5249            | 16.6977           |
| <b>13</b> | 3.2020            | 7.4318            |
| <b>14</b> | 3.6139            | 6.9442            |

Kurtosis values for the external accelerometer are consistently higher than for the internal. This is to be expected as there is more variability in vibration levels of the external signal due to the relative motion of the accelerometer and the planet gears.

The two baseline cases (Tests 1 and 2) have kurtoses not greater than 4, indicating a lack of impulsive phenomena as is to be expected. The highest kurtosis values are found to originate from the half root crack tests (Tests 3 to 6), while the quarter root crack tests (Tests 7 to 10) indicate only low levels of impulsivity. Tests 11 and 12 of the spall gear fault indicate the presence of significant impulsive phenomena, but Tests 13 and 14 in the internal signal do not. It may be concluded that at least some of the data samples appear to be correct, and further investigation is required into certain of the unexpectedly low kurtosis levels.

Due to the large number of samples taken, only a selection of time and frequency plots are presented here. A complete set of plots is presented for the undamaged 65 Nm case (Test 2) and a 65 Nm case with a faulty gear of the half root crack type (Test 4). The cases with faulty gears of quarter root crack (Test 8) and spall type (test 12) are presented only to illustrate the difference in frequency spectrum from the reference undamaged case. Refer to **Table 2** above for a complete description of test settings.

#### 4.1.1 Test 2

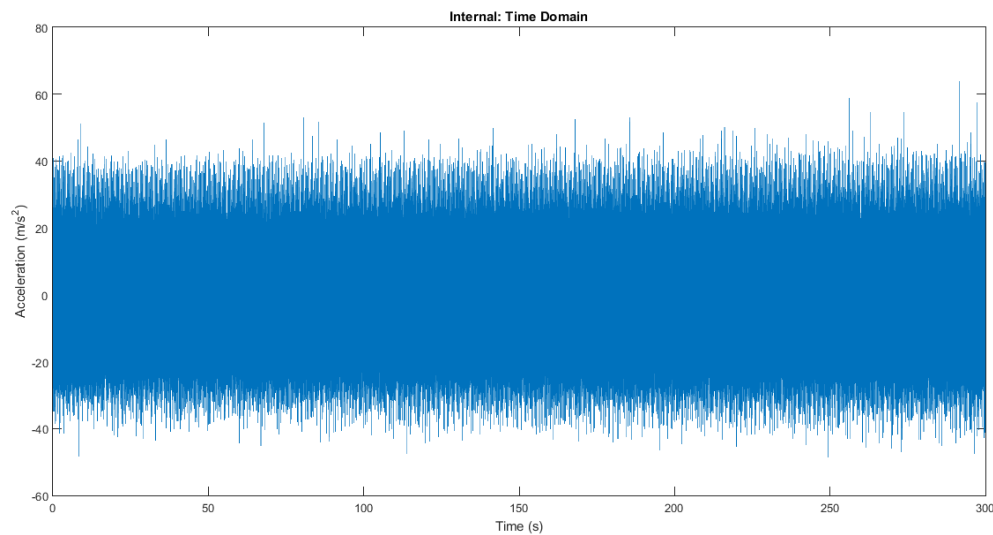


**Figure 14: The complete internal time domain signal for Test 2.**

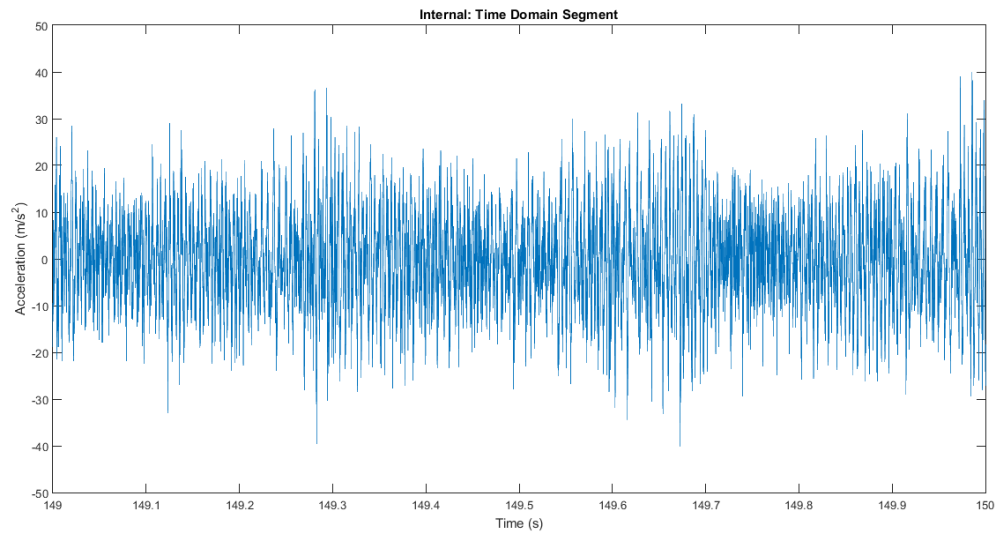


**Figure 15: A segment of the internal time domain signal for Test 2.**

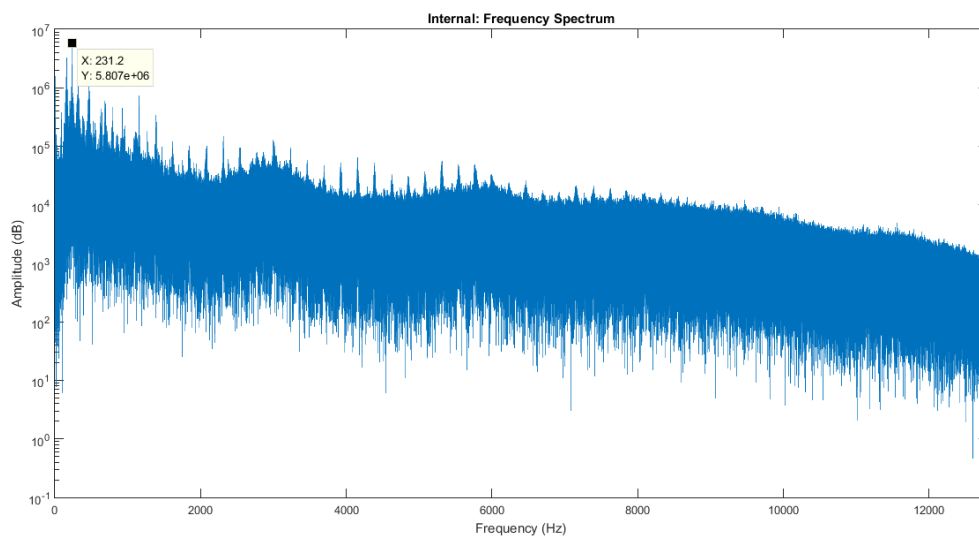


**Figure 16: Complete internal frequency spectrum for Test 2 showing RGMF.**

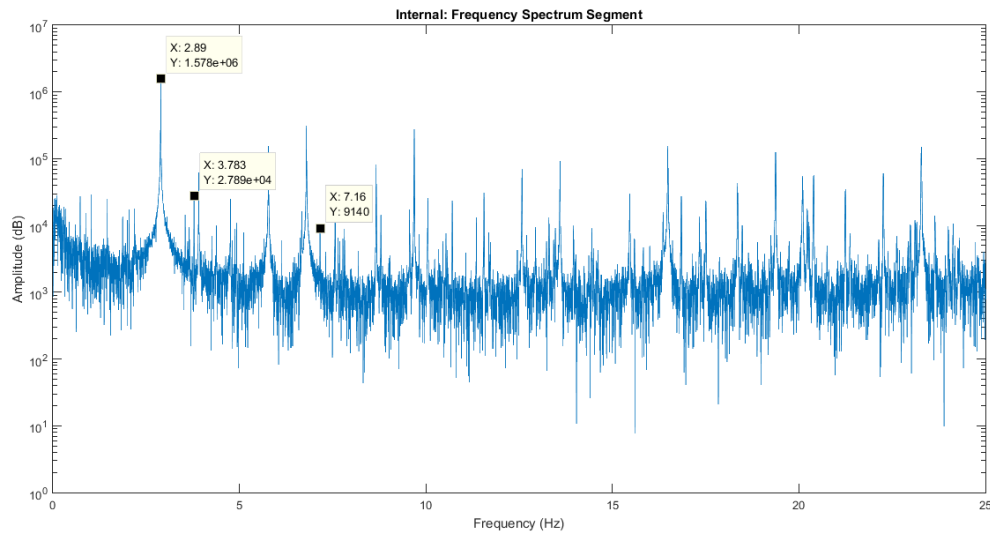


**Figure 17: A segment of the internal frequency spectrum for Test 2.**

Note that in **Figure 15** **Error! Reference source not found.** above, there are as expected no obvious jumps in acceleration, due to the lack of faulty gears. In **Figure 16** above, RGMF and SGMF (not shown) are easily identified. It may be seen in **Figure 17** that the planet carrier frequency is very dominant, but other frequencies such as input, planet, and FPGMF (not shown) are while still identifiable, not particularly dominant in the spectrum.

Additionally, the kurtosis of the raw internal time domain signal was calculated in Matlab and found to be 3.0001, which is exactly the expected value for a signal without impulsive phenomena, that is to say, without faults (de Lorenzo & Calabro, 2007).

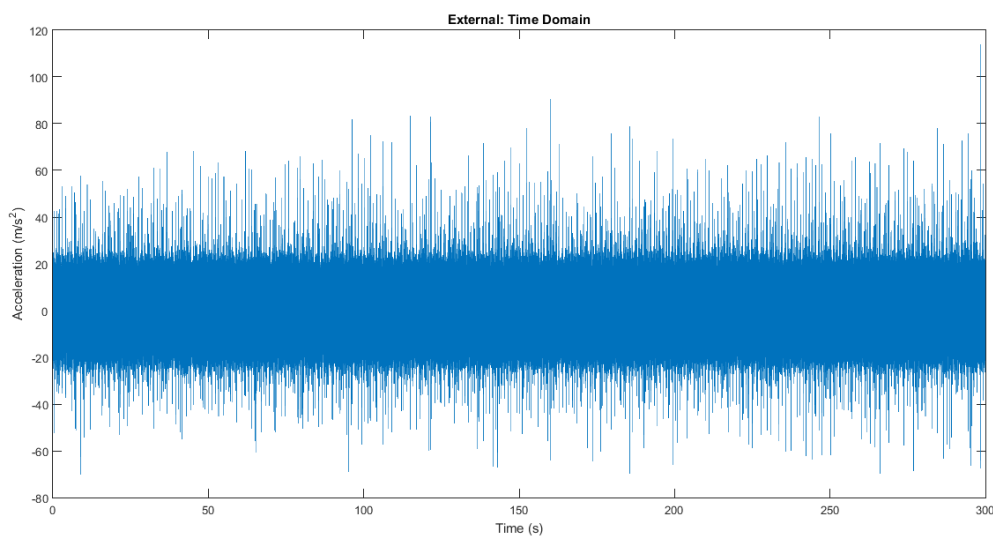


**Figure 18: The complete external time domain signal for Test 2.**

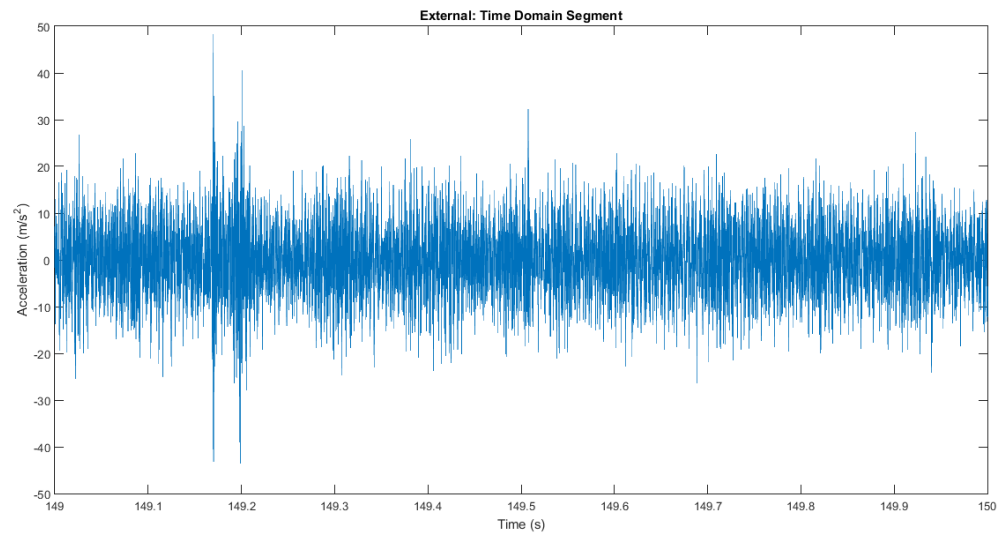


**Figure 19: A segment of the internal time domain signal for Test 2.**

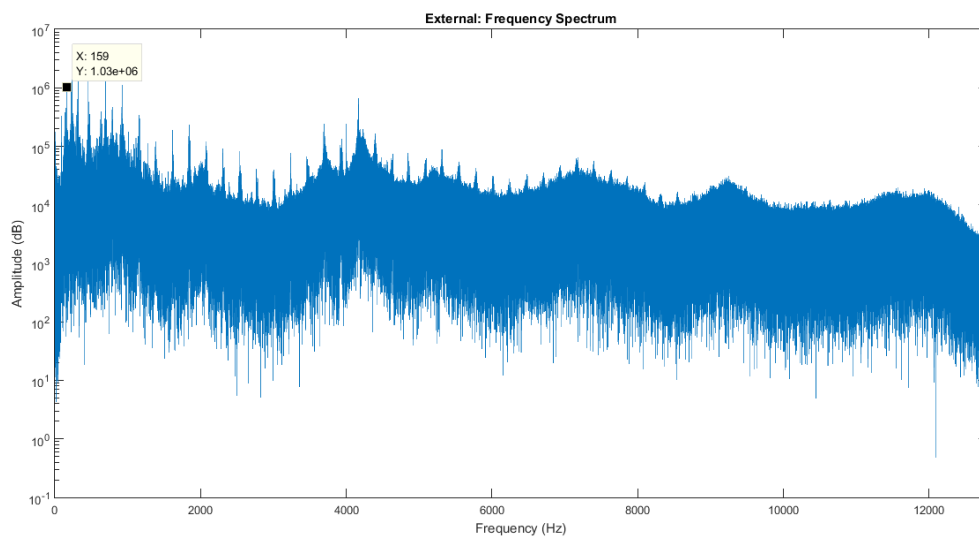


**Figure 20: Complete external frequency spectrum for Test 2 showing SGMF.**

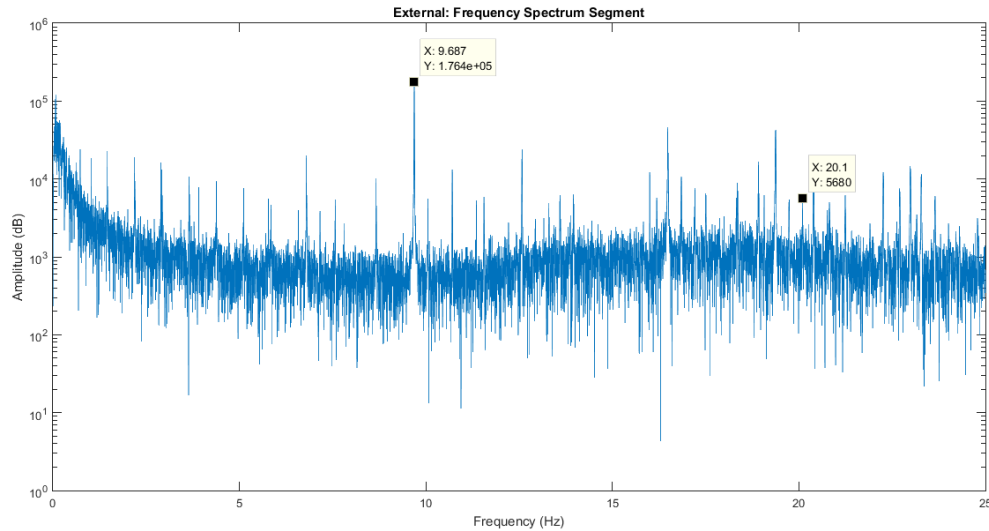


**Figure 21: A segment of the external frequency spectrum for Test 2.**

The kurtosis of the external signal for Test 2 was earlier found to be 3.8581, which while higher than that of the internal signal due to the relative motive of the planet gears to the accelerometer, is still within acceptable limits for a non-impulse signal.

As with the internal signal, identification of SGMF and RGMF in the frequency spectrum was not difficult. In **Figure 21** above the absolute spur gear frequency was dominant, and FPGMF identifiable though less obvious. Given the location of the external accelerometer, the dominance of the absolute spur gear frequency is to be expected.

#### 4.1.2 Test 4

To illustrate the appearance of a highly impulsive signal in the time domain, a segment of the time domain signal of Test 4 (half root crack fault, loaded at 65 Nm) is presented below for both internal and external signals. As Test 2 includes only undamaged gears, it is hereafter used at the baseline. The frequency spectrum difference on a linear scale between Test 4 and the baseline is shown for both signals. All kurtosis values were calculated previously in **Table 3** above.

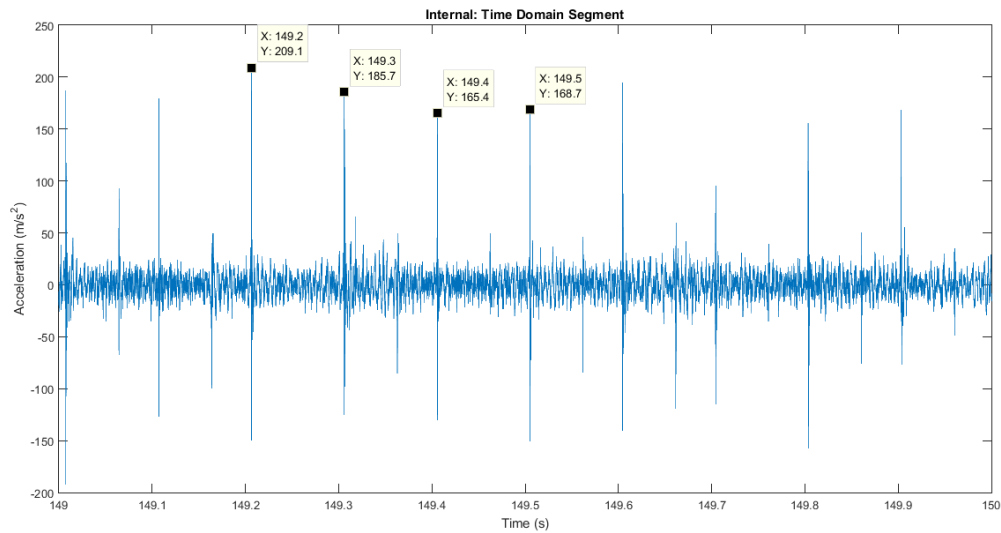


**Figure 22: A segment of the internal time domain signal for Test 4.**

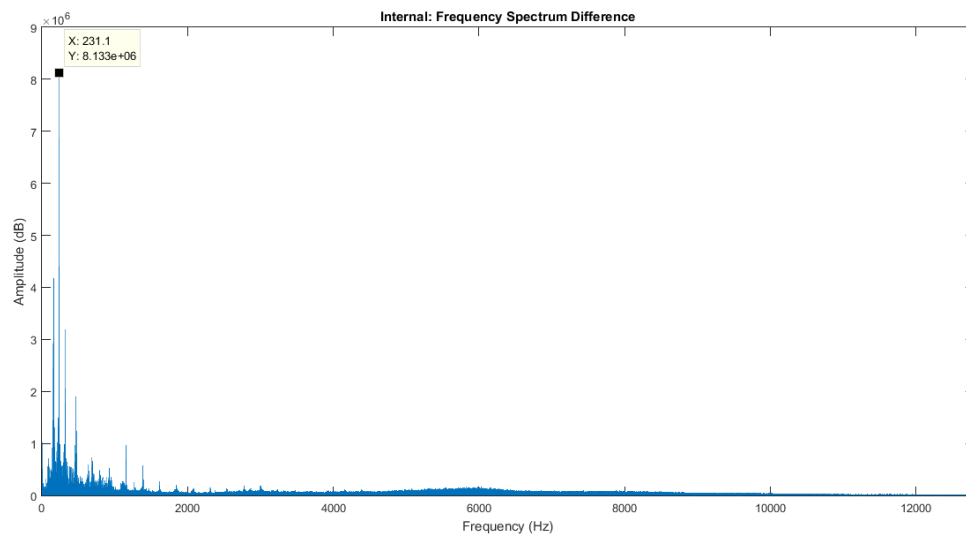


**Figure 23: The difference in the internal frequency spectrum in Test 4 from the baseline.**



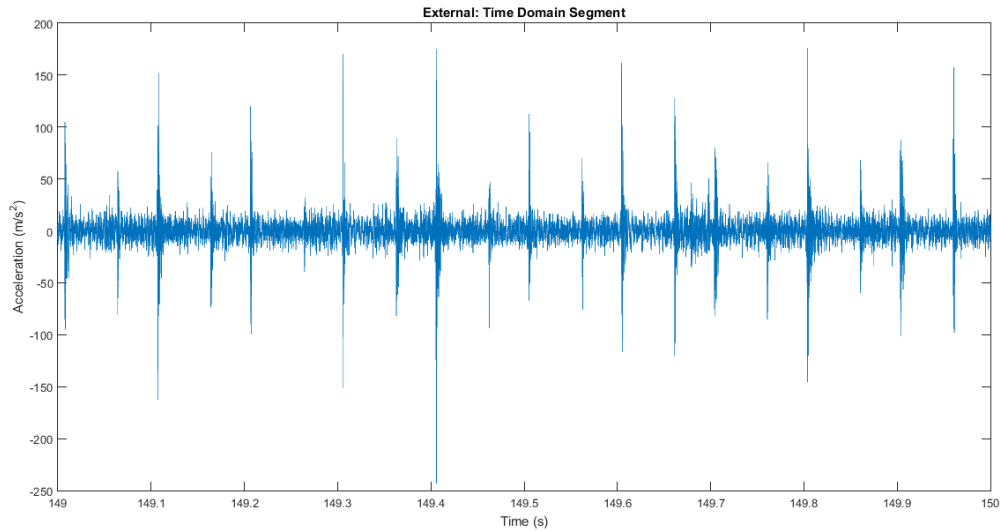


**Figure 24:** A segment of the external time domain signal of Test 4.

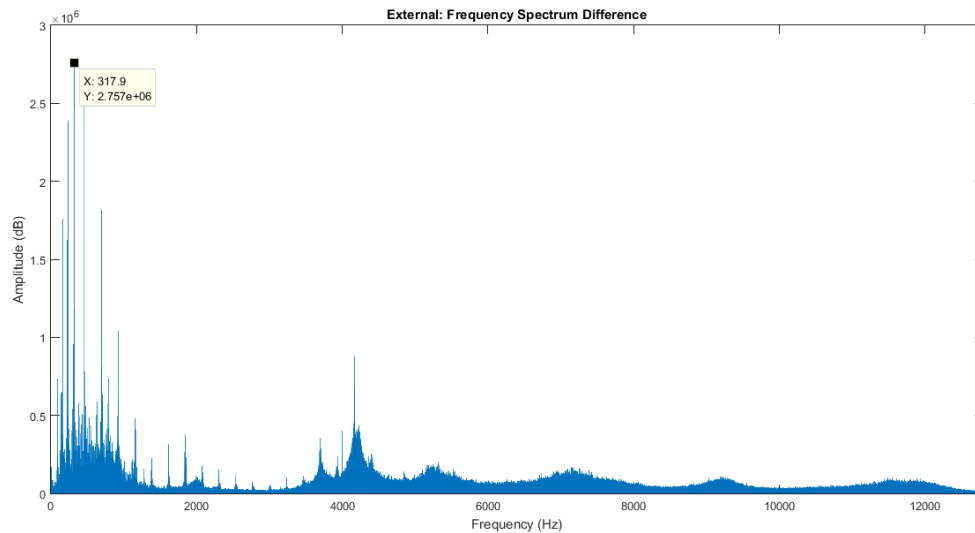


**Figure 25:** The difference in the external frequency spectrum in Test 4 from the baseline.

The kurtosis for test 4 of the internal signal is 32.2930, a value that unquestionably indicates the presence of impulsive phenomena (de Lorenzo & Calabro, 2007). The external kurtosis at 44.0813 is a similarly high value.

In **Figure 22**, the presence of the fault is extremely obvious in the internal time-domain signal, with a high impulse phenomenon occurring at a frequency of approximately 10 Hz, or half the calculated FPGMF. A moderate impulse phenomenon occurs at each midway point, and it may be reasonably concluded that these represent the alternate opening and closing of

the half root crack as it contacts the ring gear and sun gear. A similar phenomenon is observable in the external signal, but with a more variable magnitude.

In the residual frequency spectra, the most dominant component in the internal signal is again RGMF. In the external signal, shown in **Figure 25**, the second harmonic of SGMF is dominant.

#### 4.1.3 Test 8

In order that the residual frequency components at lower frequencies may be more closely examined, the difference between the internal and external frequency spectra of Test 8 and that of the baseline signal are presented below. Test 8 represents the case of the quarter root crack at 65 Nm, with the fault in the same orientation as for Test 4. Matlab code for these plots is very similar to that for previous sections and as such is not included in **Appendix D** below.

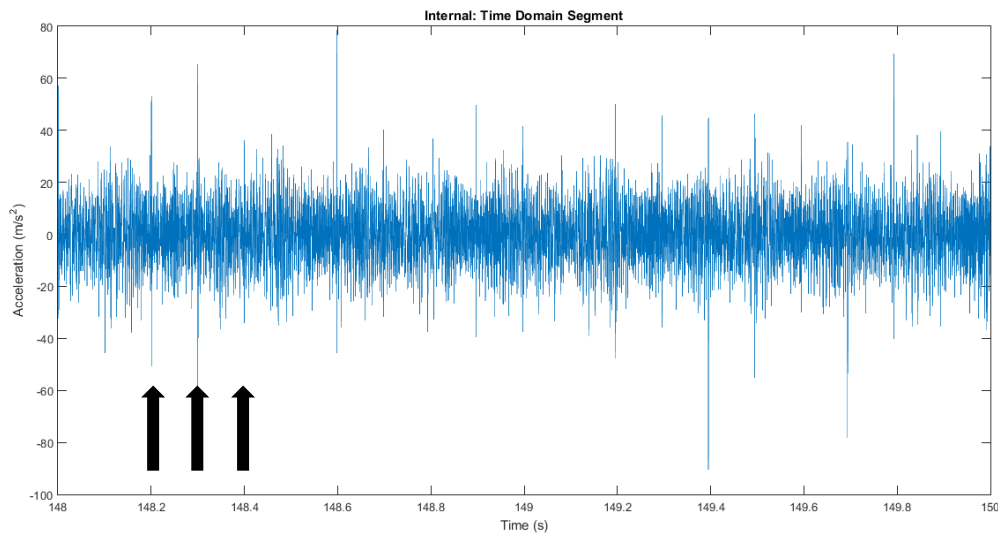


**Figure 26: A segment of the internal time domain signal for Test 8. The arrows indicate a number of fault impacts.**

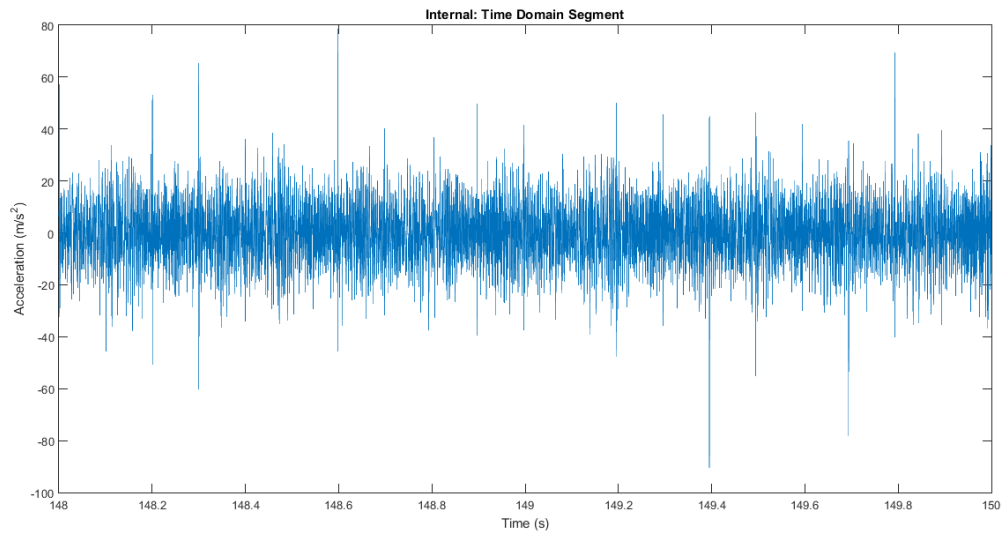


**Figure 27: A segment of the external time domain signal for Test 8.**

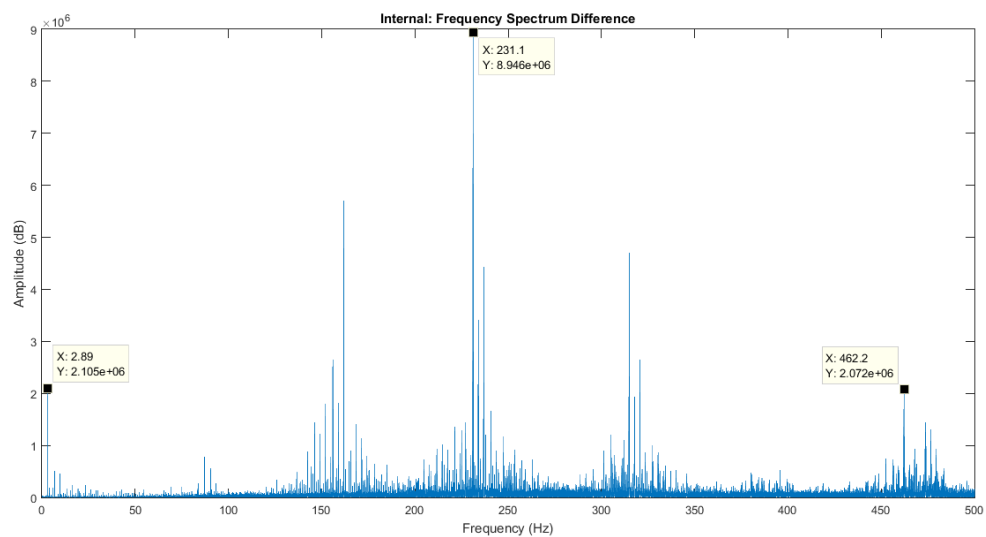


**Figure 28: The residual internal frequency spectrum of Test 8 and the baseline signal.**

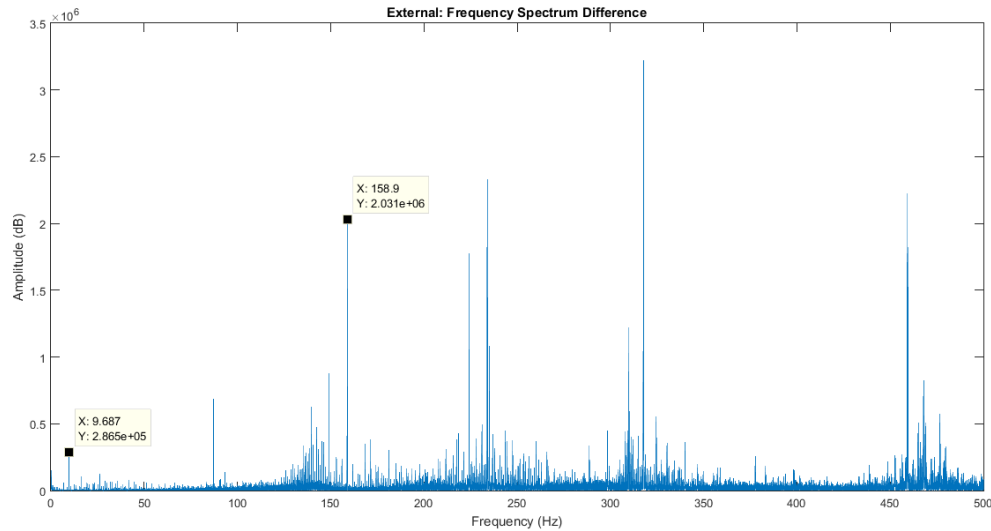


**Figure 29: The residual external frequency spectrum of Test 8 and the baseline signal.**

In the internal residual frequency spectrum shown in **Figure 28** above, dominant components were the planet carrier frequency, and RGMF and its harmonics. In the external spectrum, the planet carrier frequency was not noticeable, and the spectrum was dominated rather by the absolute sun gear frequency and SGMF.

Although in the time domain signal (**Figure 26** and **Figure 27**), the quarter root crack impact at 20.10 Hz is clear, this impulsivity was not reflected by the kurtosis value of 3.7889. The external kurtosis was somewhat greater at 4.6364, but still failed to reflect the impulsive nature of the faulty signal.

#### 4.1.4 Test 12

Finally, time domain plots of a spall gear fault test (Test 12) are given to illustrate the appearance of such faults in the internal and external time signals. In the frequency spectra, a comparison of the baseline and spall gear fault is shown for lower frequencies, to illustrate the increase in certain components in the presence of the fault.

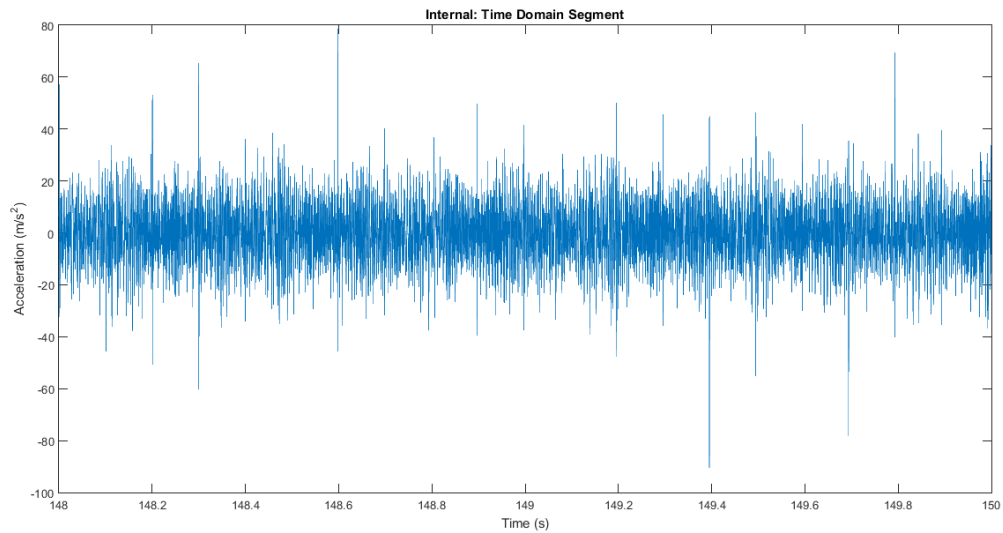


**Figure 30: A segment of the internal time signal for Test 12.**

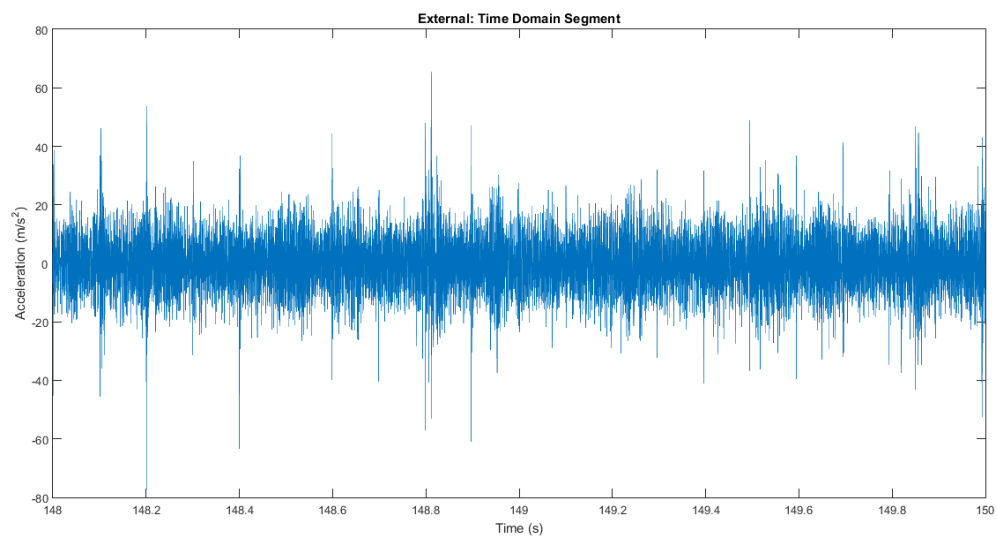


**Figure 31: A segment of the external time signal for Test 12.**

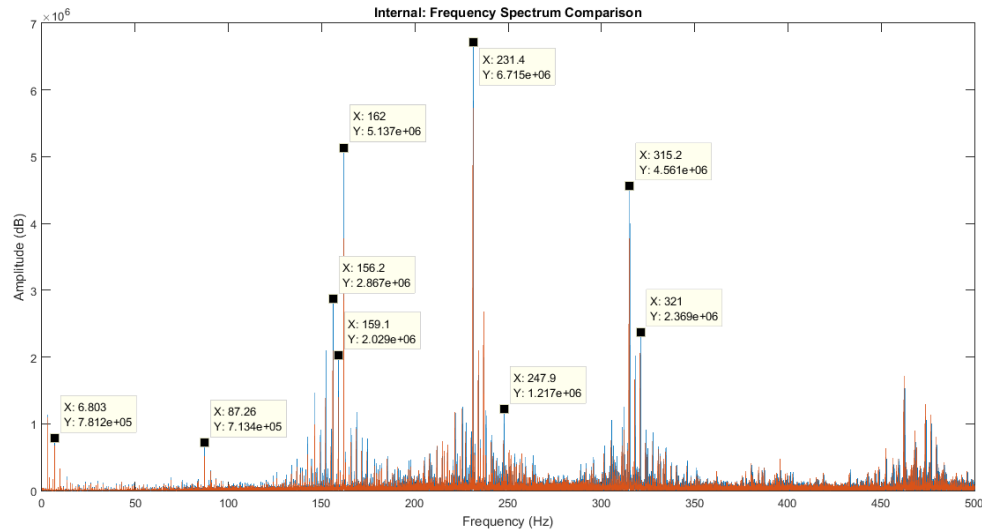


**Figure 32: The internal frequency spectrum for Test 12 (blue) and the baseline (orange).**

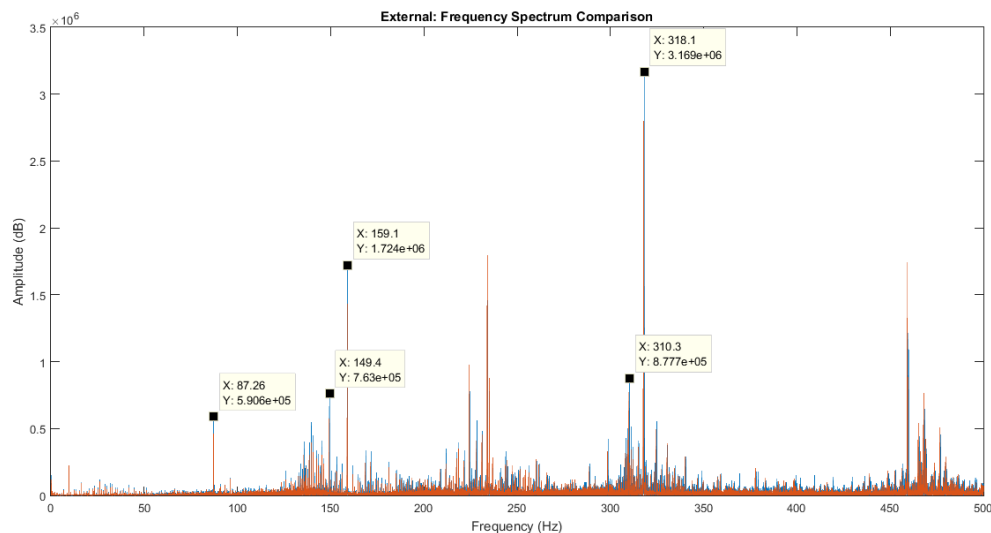


**Figure 33: The external frequency spectrum for Test 12 (blue) and the baseline (orange).**

The internal and external kurtosis values for Test 12 previously calculated are 8.5249 and 16.6977 respectively, reflecting the impulse nature of the vibration signal generated by the spall gear fault.

In the frequency spectra (**Figure 32** and **Figure 33**, the presence of the spall gear fault causes a clear increase in certain frequency components. In the internal signal, there is a particularly noticeable increase in RGMF, and in the external signal a similarly large increase

in SGMF. However, other dominant components do not correspond to gearmesh frequencies, which are difficult to locate among high harmonic and sideband components.

Matlab code used to generate these comparative plots is given in **Appendix D**.

#### **4.1.5 Some conclusions**

As a preliminary indication of the presence of impulsive phenomena in the test samples, the kurtosis values were calculated in **Table 3**. This was accurate in representing the non-impulse baseline signals, and highly impulsive half root crack gear fault cases. However, the kurtosis values did not consistently reflect the impulsive nature of signals containing quarter root crack and spall gear faults. As such, kurtosis is not an appropriate indicator of the presence of faults when the fault under investigation is not large.

Numerous time domain and frequency spectrum plots have been presented for both internal and external signals for the 65 Nm load case. In the time domain it was found that the absence or presence of a gear tooth fault was extremely obvious, somewhat more so in the internal signal than the external. However, due to the complexities of the planetary gearbox, fault frequencies were difficult to identify, as harmonics and sidebands of other meshing frequencies tend to dominate the spectrum. In particular, SGMF and RGMF frequencies are dominant.

## 4.2 The Secondary Aims

As noted in **Chapter 1** above, the secondary aim of this project is to address a number of problems associated with the implementation of the internal accelerometer. Specifically the electro-magnetic interference (EMI) thought to originate from the FRENIC-MEGA variable-frequency drive (VFD), the random signal dropouts, and as discovered in the later stages of the project, the apparent damping of the internal vibration signal. The resolution of these problems are discussed in the following sections.

### 4.2.1 Electro-magnetic interference

During previous testing it was observed that there was significant EMI present in the recorded internal vibration signal at frequencies of 14 kHz and 16 kHz (EMI at 14 kHz is visible in **Figure 34** following), which corresponded to the carrier frequency of the FRENIC-MEGA VFD. It was thus concluded that the source of the interference was likely to be the FRENIC-MEGA itself. Some attempt had been made at filtering out the EMI during signal post-processing, however it was thought to be preferable for the EMI to be eliminated at the source.

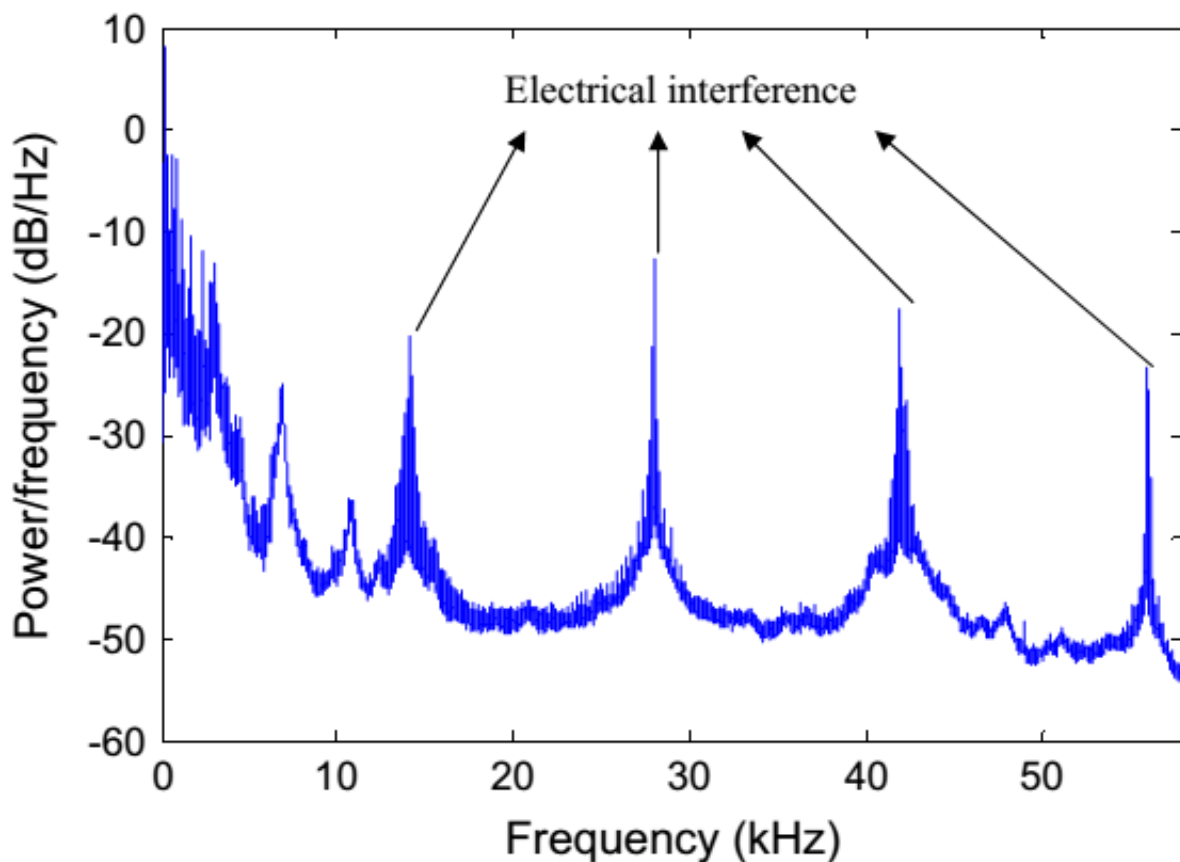


**Figure 34:** Power spectral density of an internal vibration signal recorded prior to modifications to cabling (Fan & Li, 2015).



A thorough review of existing literature on common problems associated with VFDs indicated that the most likely source of the EMI was not the VFD itself, which is responsible for relatively low levels of interference, but rather an improperly shielded or terminated cable (Anderson & Scroggins, 2012). Examination of the FRENIC-MEGA revealed that the cable running to the AC induction motor was of the single-screened aluminium foil type, which is inappropriate for such an application. Arrangements were made for this cable to be replaced with dual-screened aluminium foiled and tinned copper braid type cable. Additionally, based upon expert advice the decision was made to reduce the carrier frequency to the recommended standard value of 2 kHz.

In the frequency spectra of the raw internal data shown above there is no strong 2 kHz component. Further, other tests (not shown here) were carried out with much higher sampling frequencies, and no frequency components at 14 kHz or 16 kHz were observed. It is thus reasonable to conclude that these efforts to resolve the EMI problem originating with the FRENIC-MEGA have met with reasonable success.

#### **4.2.2 Random signal dropouts**

In the data recorded by Bligh and subsequently it was observed that in the signal from the internal accelerometer there were sudden, apparently random losses of signal for periods of no greater than one or two data points. No source of this issue was posited, although it was believed to originate from the accelerometer, slip ring, or associated cabling, and was not thought to be related to the EMI problem.

A number of attempts were made to solve the problem at the source, including resoldering all connections, redoing cabling, and replacing the accelerometer, with no noticeable improvement in the dropouts. The slip-ring manufacturer, Michigan Scientific, was also contacted, and expressed the opinion that since there was no prior report of such an issue, the random signal dropouts did not in fact originate from the slip-ring. As such efforts have since been focused on overcoming the effects of the drop-outs in post-processing.

Matlab code was developed to locate dropouts of one or two data points in width, store these locations in an array, and thus plot their incidence in the frequency spectrum, in the hope that this would allow their source to be identified. Shown in Figure 35 above, this revealed that the dropouts were not in fact random, but occurred at a fundamental frequency of 99.95 Hz, modulated at approximately 2.17 Hz. This suggests some connection between the dropouts and the mains power frequency of 50 Hz, but is not otherwise particularly useful in identifying the source.

Due to the difficulty in identifying the source, further code was developed to smooth out the dropouts in the time domain by replacing lost values with the average of the data points on either side of the dropout. As shown in Figure 36 below, the method is reasonably successful in reducing the appearance of the drop-outs in the time domain signal, and there is a corresponding drop in the kurtosis of the signal.

However, new data recorded for this report does not exhibit the same drop-out problems previously observed. The smoothing code was therefore not required here, but still may be of use in the reanalysis of samples recorded earlier. The smoothing code referred to here is given

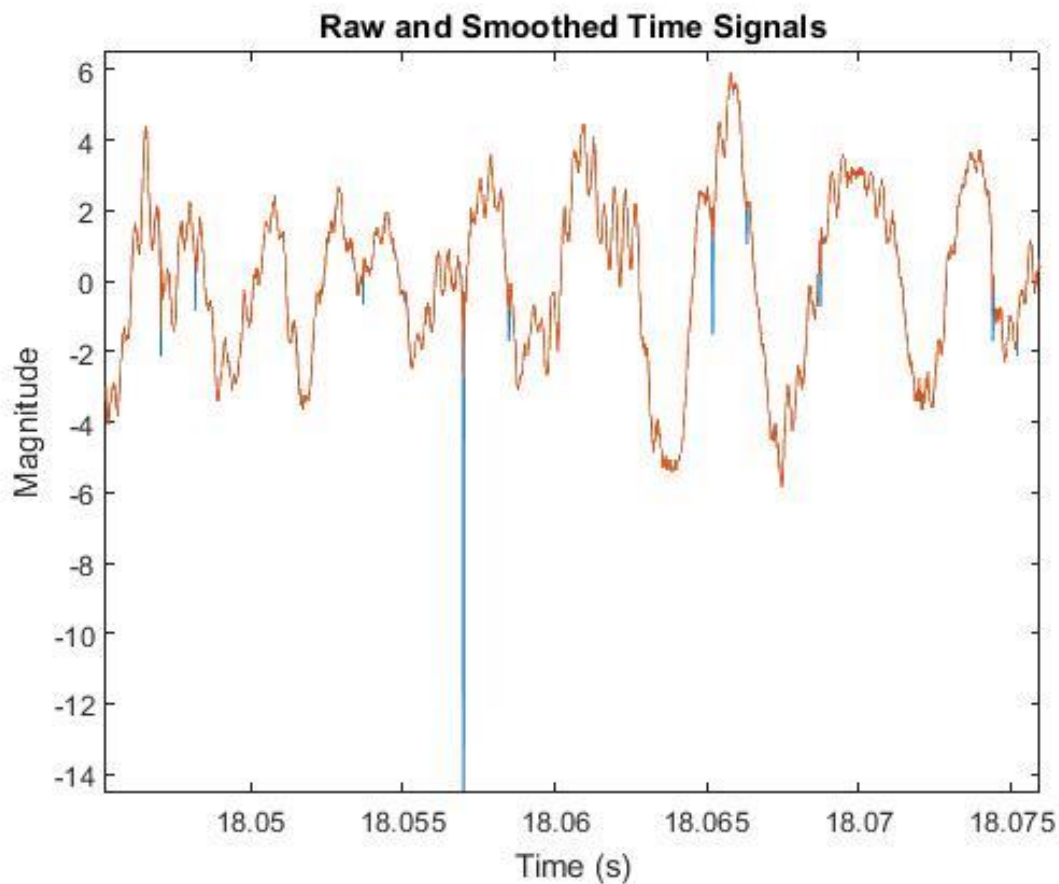


**Figure 36: Unsmoothed time signal (blue) and smoothed time signal (orange).**

in Appendix D below. The author would like to acknowledge the use of data recorded by Andrew Bligh in this section.

#### **4.2.3 Apparent signal damping**

In the first round of testing conducted, it was observed that the internal vibration signal appeared to be highly damped, and in subsequent impact tests it became apparent that the accelerometer was not responding well to external excitation. It was hypothesized that this was a result of the internal accelerometer coming loose from its mounting during the recent servicing of the hydraulic system, but due to the positioning of the accelerometer within the spur gear it was impossible to verify this without undertaking a full disassembly of the planetary gearbox.

The planetary gearbox was therefore fully disassembled. It was then realised that a section of the cabling between the accelerometer and the slip-ring has been accidentally severed at some unknown point in the past year. The apparently highly damped signal did not in fact originate from the internal accelerometer, and the apparent periodicity in the signal was a result of some peculiar electromechanical property of the gearbox.

Due to the complexity of the necessary cable route to the slip ring and difficulties in soldering the cable, the first attempt at rectifying the situation was unsuccessful. For the following attempt the orientation of the slip-ring was reversed to reduce stress on the cable, and greater care was taken in soldering. Impact tests made following this showed the expected response from the internal accelerometer, and the second round of testing produced useful samples, as shown above.

## Chapter 5

### Signal Processing


In Chapter 5 following is presented the proposed signal processing methodology for the internal and external vibration signals. The results of the preliminary signal processing attempts are given. Due to difficulties in implementation, and the large number of samples, only a selection of results is presented.

#### 5.1 Signal Processing Methodology

Due to the complexity of vibration data obtained from the external accelerometer of a planetary gearbox, as discussed in **Chapter 2** above, the signal processing methodology is much more complex than that for a parallel gearbox.

1. **Order tracking:** with respect to the frequency of the planet gears. Obtain averaged input shaft speed and thus derive other significant frequencies (as in **Appendix A** following).
2. **Time-synchronous averaging:** with respect to the planet gears.
3. **Demodulation:** in order to determine the reference point to be used in window mapping.
4. **Windowing:** in accordance with McFadden's method, using a rectangular or preferably Hanning window.
5. **Mapping windows:** using the planet-ring mesh sequence given in **Appendix A**, reconstruct a complete vibration signature of each planet gear.
6. **Vibration signal analysis:** standard techniques may be applied to the reconstructed signal.

One of the primary advantages of the internal accelerometer technique is the reduction in complexity of the required signal processing. Reconstruction of the planet gear vibration signature is not required and the raw signal may have TSA applied directly following order tracking. The proposed procedure is as follows;

1. **Order tracking:** with respect to the frequency of the planet gears. Obtain averaged input shaft speed and thus derive other significant frequencies (as in **Appendix A** following).
2. **Time-synchronous averaging:** with respect to the planet gears. 
3. **Vibration signal analysis:** standard techniques may be applied to the reconstructed signal.

In this report, the large sample size, extremely long processing times, and difficulties with implementation have unfortunately prevented the carrying out of these proposed signal processing methodologies. In the following section, order tracking has been carried out on a small subset of the recorded data samples, and a preliminary discussion of the effectiveness of the method is given.

## 5.2 Preliminary Results

Matlab codes for order tracking and generating the following plots may be found in **Appendix D**. As in **Chapter 4**, plots given below are for the 65 Nm load case, specifically the baseline signal (Test 2) and a half root crack gear fault case (Test 4). Order tracking was carried out with respect to the planet gears. Note that the input shaft speed derived from the raw data for this load case was 3.785 Hz.

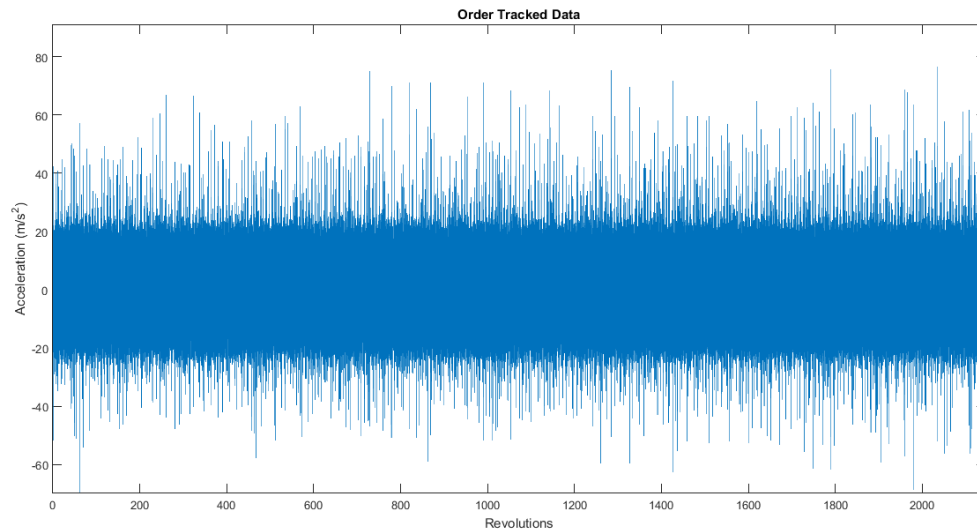


**Figure 37: External order-tracked data for Test 2. The x-axis is in shaft revolutions.**

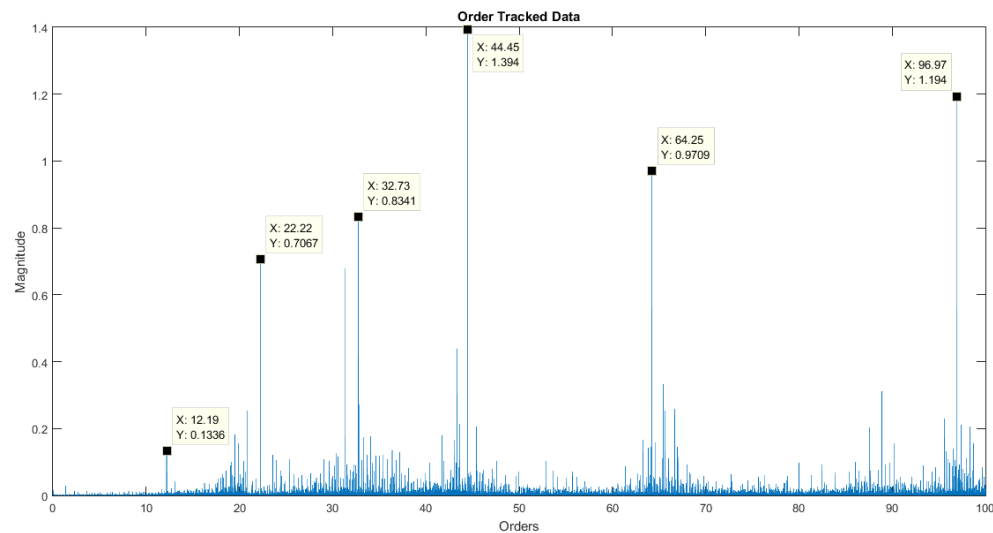


**Figure 38: External order-tracked frequency data for Test 2. Note that the x-axis is in shaft orders.**

Input shaft speed as calculated by the order-tracking code was 3.7833 Hz, very close to the value of 7.385 Hz derived from the unprocessed data. After order tracking, the sample in the “time” domain is not significantly different, due to the low variability of the input speed as demonstrated by the close correlation of the raw and order-tracked input shaft speeds.

For the external data, the effect of order-tracking is more obvious in the “frequency” spectrum. Noise levels in **Figure 38** above are significantly lower than in the corresponding raw

data plot. The sidebands that previously interfered with the identification of mesh and fault frequencies also appear to have been reduced.

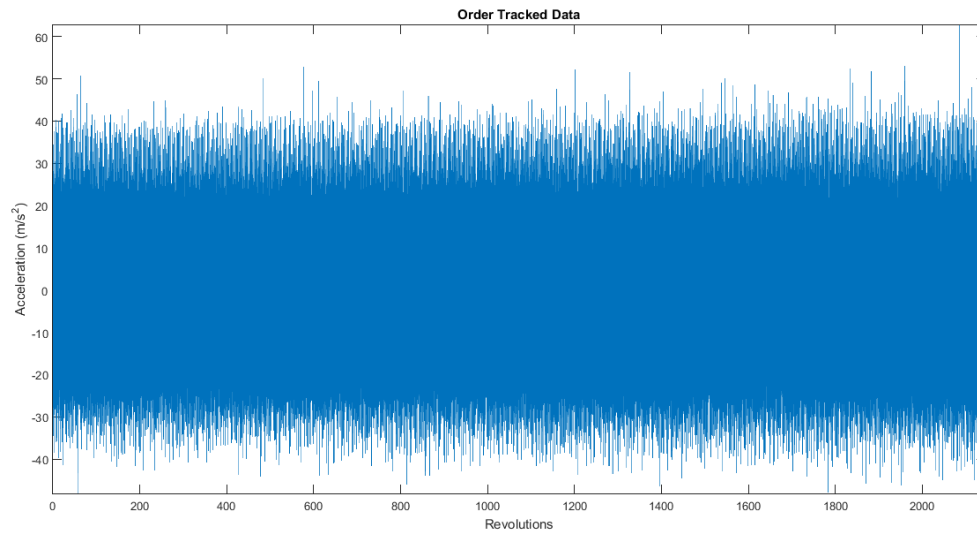


**Figure 39: Internal order-tracked data for Test 2.**

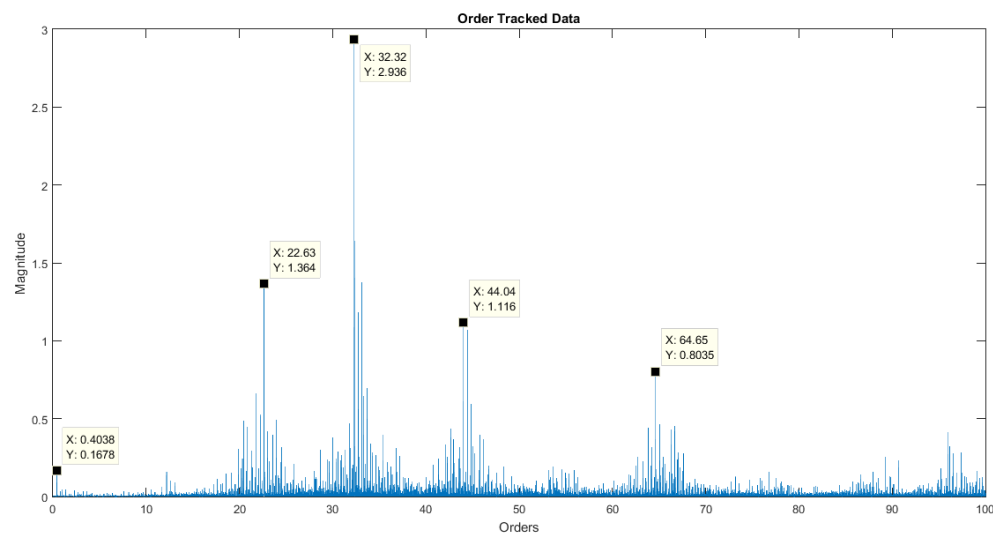


**Figure 40: Internal frequency data for Test 2.**

As in the case of the external data, there is minimal discernible difference between the raw time domain data and the order-tracked “time” domain data, due to the low variability in the input shaft speed.

There are noticeable difference between the external and internal order-tracked frequency data. In the internal data, the component at ~ 64 shaft orders is significantly lower,

and the dominant component at  $\sim 97$  shaft orders is missing entirely. These differences are much more apparent in the order-tracked data than in the raw data.

Below is presented a comparison of the internal and external order-tracked samples between Test 4 – a half root crack fault at 65 Nm – and the baseline test. It was found in order-tracking that the input shaft speed was 3.7833 Hz, again showing a good correspondence to the speed calculated from the raw data, and proving that there was a low variability in the input shaft speed over the duration of the sample.

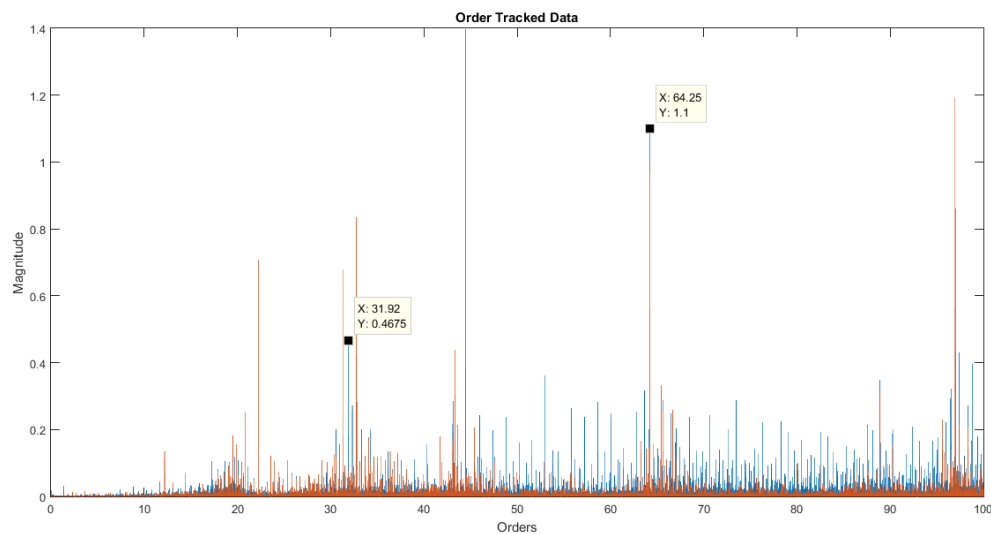


**Figure 41: Comparison of external order-tracked data for Test 4 (blue) and the baseline (orange).**

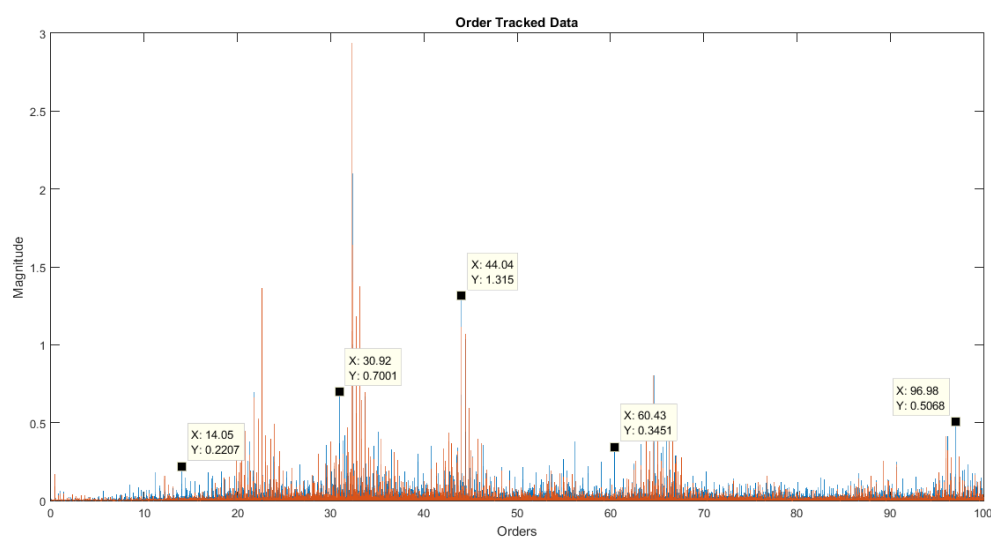


**Figure 42: Comparison of internal order-tracked data for Test 4 (blue) and the baseline (orange).**



As expected, there is a strong correlation between the frequency data for the half root crack gear fault and baseline order-tracked samples for both external (**Figure 41**) and internal (**Figure 42**) data. In the external plot it may be observed that the faulty gear produced additional low-level components throughout the spectrum. This was not observed in the internal data, which displayed rather changes in the level of existing dominant components.

## Chapter 6

### Conclusion

In Chapter 6 following is summarized the results and outcomes of the primary and secondary aims of the project. Suggestions for future work on the primary project aim are given. A brief discussion of the future of the internal accelerometer technique with emphasis on the use of wireless technologies is conducted.

#### 6.1 Some Conclusions


Presented in Chapter 4 was a complete calculation of kurtosis values for all data samples, and a representative selection of plots for the 65 Nm loading case. It was found that while kurtosis is an effective indicator of strong faults, and equally correct in representing the absence of impulsive phenomena, for intermediate-sized faults such as the quarter root tooth and the spall it was significantly less reliable. Therefore it may be concluded that kurtosis is not a appropriate tool for detecting faults in all cases.

An examination of the time domain showed that the impulses resulting from the presence of the fault were easily detectable through observation, for all three fault types tested. Not shown was the reverse orientations of each fault type, but the impulses were found to be equally obvious. In small-scale applications, therefore, observation of the raw time domain may be of use in identifying gear faults. However in large-scale operations such as wind turbine farms, where automation of fault detections systems is necessary, this method is not particularly viable.

Further, while it is possible to identifying manually many of the meshing and fault frequencies in the frequency spectra shown in Chapter 4, these components are often not

dominant, with the spectrum being dominated rather by harmonics and sidebands. It is therefore obvious that analysis of the raw frequency data is not the best solution for identifying the presence of faults.

Consequently, some preliminary attempts were made at signal processing of both the internal and external data. Due to the very large sample sizes, resulting large processing times, and difficulties with implementation, it was not possible to progress the signal processing further than the order-tracking stage of the methodology as outlined in Chapter 5.

As a measure of the variation in input shaft speed, the speed as calculated from the tenth harmonic of the FFT of the tachometer signal in the raw data was compared to that calculated through order tracking. The **lack of smearing of frequency components** in the tachometer signal, and **the good correlation between the two values indicate** a relatively low variability in the input shaft speed. 

Order-tracking with reference to the planet gear was carried out on a representative selection of test samples, namely the baseline 65 Nm load case and a corresponding half root crack gear fault case. It was observed that there were minimal differences between the raw and order-tracked data in terms of time, a result of the abovementioned low variability in input shaft speed.

In terms of frequency, order-tracking was highly useful in reducing the noise levels in the spectrum. The spectral difference between internal and external data were also more clear in the order-tracked data. However, as no further signal processing methods were able to be implemented, the major conclusion that may be drawn from this is that order-tracking is of use in reducing noise levels. No diagnosis of faults could be made at this point in the signal processing.

In reference to the secondary aims of the project. The electro-magnetic interference problem originating from the FRENIC-MEGA variable frequency drive was successfully diagnosed, and changes implemented in the set-up of the UNSW large gearbox test rig have proven effective in eliminating the problem. A signal-processing method was developed to resolve the “randon” signal drop-out problem, although as new data samples were not subject to this issue, the method has not been made use of here. However, it may be of use in reanalysis of pre-existing data sets, should the need arise. Further, a complete disassembly of the planetary gearbox has been carried out and repairs made to the faulty internal accelerometer cable, a

measure that has proven successful in resolving the apparent damping of the **interl** vibration signal.

Finally, it may be concluded that looking forward the primary contribution of this project to the internal accelerometer technique does not lie with any advances in understanding of its usefulness, or with improvements made to existing signal processing methods. Rather, the resolution of the numerous issues related to the UNSW test rig will prove of great benefit in future work. Further, the author would like to note that the new data samples recorded in the course of this project are of a high quality and are not subject to the issues previously affecting data taken from the test rig. As the data samples span a comprehensive range of fault types, orientations, and load conditions, they should prove of great value to any researcher investigating the internal accelerometer technique in the future.

## **6.2 Future Work**

There is immense scope for further work into the internal accelerometer technique in general, and its application to the UNSW test rig specifically. Given that the numerous issues affecting the test rig have now been satisfactorily resolved, more data samples at a broader range of load conditions and with different gear fault types would be of great value. Applying a broader range of load conditions is however contingent on the resolution of the issue concerning the use of drive belts in the test rig.

A preliminary methodology for signal processing and analysis of the internal and external vibration data has been given in Chapter 5 above. Scope for future work into the further development of this methodology is great. Also, improvement of the signal processing codes developed by Shao would be of great value to the internal accelerometer technique moving forward (Shao, 2015).

## **6.3 The Future of the Internal Accelerometer**

As noted by de Smidt, implementation of the internal accelerometer technique in industry is greatly inhibited by the necessity to make major changes to the gearbox in order to accommodate the slip-ring (de Smidt, 2009). However, wireless technologies have now advanced to the point that the implementation of a wireless transmitter for the internal accelerometer is not entirely unfeasible. In fixed installations such as wind turbine farms the modifications required for such a system would not be greatly detrimental.

Such an implementation has now been made as part of the i-Mass project. Although publications are still forthcoming, Hilbert has noted that preliminary analysis suggests that the use of the wireless transmitted has been successful (Hilbert, 2015). The author would like to note at this point that although this project relies on the use of the Michigan Scientific slip-ring, the future of the internal accelerometer technique lies rather with the use of the wireless transmitter.

## Chapter 7

## References

In Chapter 7 following is listed the references. Note that any uncredited images in this report belong to the author.

Anderson, E., and Scroggins, C., “Correcting problems caused by variable frequency drives,” H.E. Anderson Company, 2012.

Bligh, A., “Design, manufacture and testing of a planetary gearbox rig for the purpose of internal vibration based condition monitoring,” B.E. Thesis, School of Mech. and Manf. Engineering, UNSW, Sydney, 2012.

Brüel & Kjær. *Miniature piezoelectric CCLD accelerometer, insulated base, incl. cable - Brüel & Kjær*. [online] Bksv.com. 2015. Available at: <http://www.bksv.com/Products/transducers/vibration/accelerometers/accelerometers/4394?tab=accessories&productoption=-4394---> [Accessed 7 Nov. 2015].

Fan, Z., and Li, H., “A hybrid approach for fault diagnosis of planetary bearings using an internal vibration sensor,” *Measurement*, Vol. 64, 2015, pp. 71-80.

Forrester, B. D., “A method for the separation of epicyclic planet gear vibration signatures,” *Third International Conference on Acoustical and Vibratory Surveillance Methods and Diagnostic Techniques*, 1998.

Forrester, D., and Blunt, D., “Analysis of epicyclic gearbox vibration,” HUMS 2003 Conference [CD-ROM], 2003.

Frith, J. *GCube report on wind turbine gearbox downtime*. [online] Maritimejournal.com. 2 Feb. 2015. Available from: <http://www.maritimejournal.com/news101/insurance,-legal-and-finance/gcube-report-on-wind-turbine-gearbox-downtime> [Accessed 8 Nov. 2015].

Hilbert, M., Schütz, M., Boos, D., Bernet, C., Baltes, R., Bartnitzki, T., Kleine-Rüschkamp, L., Küch, C., Jacek, A., Nienhaus, K., “i-MaSS: Approach for vibration measurements on rotating machine parts in gearboxes of wind turbines,” ComDem2013, 2013.

Hilbert, M. “PhD student exchange UNSW: overview of research,” The University of New South Wales, 24 Aug. 2015.

Howard, I. M., “An investigation of vibration signal averaging of individual components in an epicyclic gearbox,” Department of Defence: Defence Science and Technology Organisation: Aeronautical Research Laboratory Propulsion Report, Vol. 185, 1991.

Lei, Y., Lin, J., Zuo, M. J., and He, Z., “Condition monitoring and fault diagnosis of planetary gearboxes: A review,” *Measurement*, Vol. 48, 2014, pp. 292-305.

de Lorenzo, F., and Calabro, M. “Kurtosis: a statistical approach to identify defect in rolling bearings,” *Proceedings of the First International Conference on Marine Research and Transportation*, 2007.

Lyon, R. H. *Machinery Noise and Diagnostics*, Butterworth Publishers, Boston, 1987.

McFadden, P. D., “A model for the extraction of periodic waveforms by time domain averaging”, Department of Defence: Aeronautical Research Laboratory: Aero Propulsion Technical Memorandum, Vol. 435, 1986.

McFadden, P. D., “A revised model for the extraction of periodic waveforms by time domain averaging”, *Mechanical Systems and Signal Processing*, Vol. 1, 1987, pp. 83-95.

McFadden, P. D., “A technique for calculating the time domain averages of the vibration of the individual planet gears and the sun gear in an epicyclic gearbox,” *Journal of Sound and Vibration*, Vol. 144, No. 1, 1991, pp. 163-172.

McFadden, P. D., “Window functions for the calculation of the time domain averages of the vibration of the individual planet gears and sun gear in an epicyclic gearbox,” *Journal of Vibration and Acoustics*, Vol. 116, April 1994, pp. 179-187.

McFadden, P. D., and Smith, J. D., “A signal processing technique for detecting local defects in a gear from the signal average of the vibration”, *Proceedings of the Institution of Mechanical Engineers, Part C: Journal of Mechanical Engineering Science*, Vol. 199, 1985, pp. 287-292.

OROS. *OR35, 8 ch. Integrated Analyzer*. [online] Oros.com. 2015. Available at: <http://www.oros.com/3891-or35-integrated-analyzer.htm> [Accessed 7 Nov. 2015].

Princeton. *The epicyclic gearbox*. [online] Princeton.edu. 2010. Available at: <https://www.princeton.edu/~maelabs/hpt/pro/epicyclic.htm> [Accessed 8 Nov. 2015].

Randall, R. B., *Vibration-based Condition Monitoring: Industrial, Aerospace and Automotive Applications*, John Wiley & Sons, Chichester, UK, 2011.

Randall, R. B., and Antoni, J. “Rolling element bearing diagnostics – a tutorial,” *Mechanical Systems and Signal Processing*, Vol. 25, No. 2, 2011, pp. 485-520.

Shao, T., “Vibration signal analysis and experimentation of planetary gearbox,” B.E. Thesis, School of Mech. and Manf. Engineering, UNSW, Sydney, 2015.

de Smidt, M. R., “Internal vibration monitoring of a planetary gearbox,” M.E. Thesis, Department of Mech. and Aero. Engineering, University of Pretoria, Pretoria, South Africa, 2009.

Smith, W., Deshpande, L., Randall, R., and Li, H., “Gear diagnostics in a planetary gearbox: a study using internal and external vibration signals,” *The International Journal of Condition Monitoring*, Vol. 3, No. 2, 2013, pp. 1-6.

Stewart, R. M., “Some useful data analysis techniques for gearbox diagnostics,” *Proceedings of the Meeting on the Applications of Time Series Analysis*, 1977.

Sweeney, P. J., and Randall, R. B. 'Gear transmission error measurement using phase demodulation', *Proceedings of the Institution of Mechanical Engineers Part C: Journal of Mechanical Engineering Science*, Vol. 210, 1996, pp. 201-213.

Wu, B., Saxena, A., Khawaja, T. S., Patrick, R., Vachtsevanos, G., and Sparis, P., “An approach to fault diagnosis of helicopter planetary gears,” *Autotestcon 2004 Proceedings*, 2004, pp. 475–481.



Yip, L. “Analysis and modelling of planetary gearbox vibration data for early fault detection”, ME Thesis, Graduate Department of Mechanical and Industrial Engineering, University of Toronto, Toronto, Canada, 2011.

## Chapter 8

## Appendices

In Appendix A is given information concerning the configuration of the gearbox including gear tooth numbers, and all useful calculations regarding gearbox and gearmesh frequencies. Significant frequencies resulting from these calculations are given for both the 50 Nm and 65 Nm tests.

In Appendix B is given the specifications of the Brüel & Kjær 4394 accelerometer used in the set-up of the NVGate template.

In Appendix C is given a summary of the test conditions, including the FRENIC-MEGA and NVGate settings.

In Appendix D is given all Matlab code used in this project.

## Appendix A

### A.1 Gear tooth numbers

**Table 4: Gear tooth numbers.**

| Type of Gear | Symbol       | Number of Teeth |
|--------------|--------------|-----------------|
| Pinion       | $N_{pinion}$ | 42              |
| Spur         | $N_{spur}$   | 55              |
| Ring         | $N_r$        | 80              |
| Planet       | $N_p$        | 23              |
| Sun          | $N_s$        | 34              |

## A.2 Gearbox frequency equations

In the following equations,  $f_{input}$  is the frequency of the input shaft as determined from the once-per-revolution tachometer signal for each sample. The author acknowledges the work of Shao in the derivation of the following equations (Shao, 2015).

Carrier frequency  $f_c$ :

$$\begin{aligned} f_c &= f_{input} \left( -\frac{N_{pinion}}{N_{spur}} \right) \\ &= f_{input} \left( -\frac{42}{55} \right) \\ &= -0.76f_{input} \end{aligned}$$

Absolute planet frequency  $f_p$ :

$$\begin{aligned} f_p &= f_c \left( 1 - \frac{N_r}{N_p} \right) \\ &= f_{input} \left( -\frac{42}{55} \right) \left( 1 - \frac{80}{23} \right) \\ &= 1.89f_{input} \end{aligned}$$

Planet frequency relative to the carrier  $f_{p/c}$ :

$$\begin{aligned} f_{p/c} &= f_c \left( -\frac{N_r}{N_p} \right) \\ &= f_{input} \left( -\frac{42}{55} \right) \left( -\frac{80}{23} \right) \\ &= -2.66f_{input} \end{aligned}$$

Absolute sun frequency  $f_s$ :

$$\begin{aligned} f_s &= f_c \left( \frac{N_r}{N_s} + 1 \right) \\ &= f_{input} \left( -\frac{42}{55} \right) \left( \frac{80}{34} + 1 \right) \\ &= 2.56f_{input} \end{aligned}$$

Sun frequency relative to the carrier  $f_{s/c}$ :

$$f_{s/c} = f_c \left( \frac{N_r}{N_s} \right)$$

$$\begin{aligned} &= f_{input} \left( -\frac{42}{55} \right) \left( \frac{80}{34} \right) \\ &= -1.80 f_{input} \end{aligned}$$

### A.3 Gearmesh frequency equations

In the following equations,  $n$  is the number of planet gears. The author acknowledges the work of Shao in the derivation of the following equations (Shao, 2015).

Spur gear mesh frequency  $SGMF$ :

$$\begin{aligned} SGMF &= f_{input} N_{pinion} \\ &= 42 f_{input} \end{aligned}$$

Ring gear mesh frequency  $RGMF$ :

$$\begin{aligned} RGMF &= f_c N_r \\ &= 61.1 f_{input} \end{aligned}$$

Planet pass frequency  $PPF$ :

$$\begin{aligned} PPF &= f_c n \\ &= 2.29 f_{input} \end{aligned}$$

Faulty planet gear mesh frequency  $FPGMF$ :

$$\begin{aligned} FPGMF &= 2 f_{p/c} \\ &= 5.31 f_{input} \end{aligned}$$

#### A.4 Significant frequencies

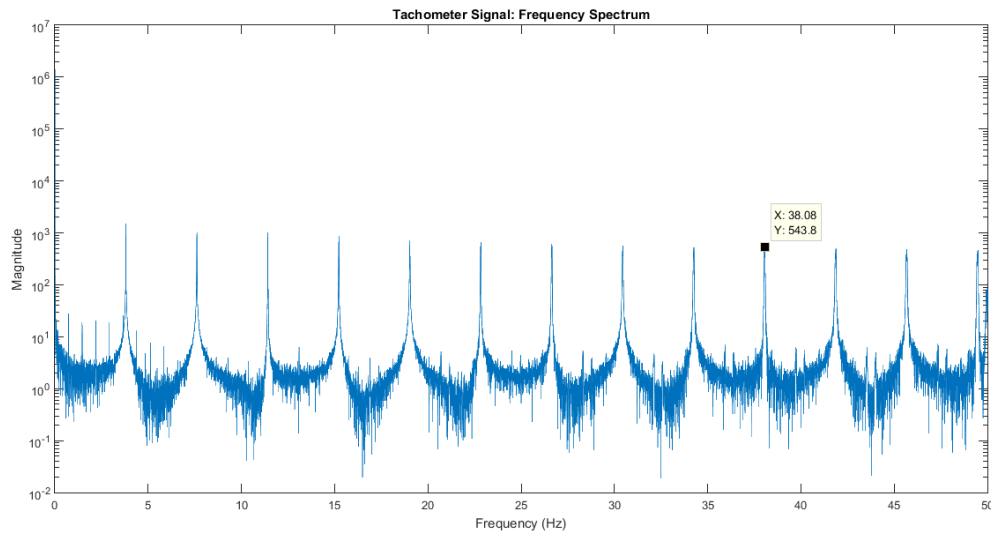


**Figure 43: FFT of the tachometer signal for Test 1.**

The average input frequencies  $f_{input}$  for each of the fourteen tests are determined from the tenth harmonic of the FFT of the tachometer signals (an example is shown in **Figure 43** above), and are listed in **Table 5** following.

**Table 5: Average input frequencies.**

| Test No.       | Input Frequency (Hz) | Test No.       | Input Frequency (Hz) |
|----------------|----------------------|----------------|----------------------|
| 1              | 3.808                | 2              | 3.783                |
| 3              | 3.808                | 4              | 3.783                |
| 5              | 3.809                | 6              | 3.787                |
| 7              | 3.807                | 8              | 3.783                |
| 9              | 3.808                | 10             | 3.785                |
| 11             | 3.809                | 12             | 3.787                |
| 13             | 3.810                | 14             | 3.788                |
| <b>Average</b> | <b>3.808</b>         | <b>Average</b> | <b>3.785</b>         |

The average input frequency of the seven tests for both the 50 Nm and 65 Nm loading cases are used in determining the significant frequencies listed in **Table 6** below.

**Table 6: Significant frequencies.**

| Frequency    | 50 Nm Tests (Hz) | 65 Nm Tests (Hz) |
|--------------|------------------|------------------|
| $f_c$        | -2.91            | -2.89            |
| $f_p$        | 7.21             | 7.16             |
| $f_{p/c}$    | 10.11            | 10.05            |
| $f_s$        | -9.75            | -9.69            |
| $f_{s/c}$    | -6.84            | -6.80            |
| <b>SGMF</b>  | 159.94           | 158.97           |
| <b>RGMF</b>  | 232.67           | 231.26           |
| <b>PPF</b>   | 8.72             | 8.67             |
| <b>FPGMF</b> | 20.22            | 20.10            |



**A.5 Planet tooth mesh count for the ring gear****Table 7: Tooth mesh count between a planet gear and the ring gear.**

| <b>Revolution</b> | <b>Planet Tooth Number</b> |
|-------------------|----------------------------|
| 1                 | 1                          |
| 2                 | 12                         |
| 3                 | 23                         |
| 4                 | 11                         |
| 5                 | 23                         |
| 6                 | 10                         |
| 7                 | 21                         |
| 8                 | 9                          |
| 9                 | 20                         |
| 10                | 8                          |
| 11                | 19                         |
| 12                | 7                          |
| 13                | 18                         |
| 14                | 6                          |
| 15                | 17                         |
| 16                | 5                          |
| 17                | 16                         |
| 18                | 4                          |

|    |    |
|----|----|
| 19 | 15 |
| 20 | 2  |
| 21 | 14 |
| 22 | 2  |
| 23 | 13 |
| 24 | 1  |

**Appendix B****Table 8: Specifications of the Brüel & Kjær 4394 accelerometer (Brüel & Kjær, 2015).**

|  |               |
|--|---------------|
| <b>Frequency range</b>   | 1 to 25000 Hz |
| <b>Sensitivity</b>   | 10 mV/g       |
| <b>Temperature range</b>   | -50 to 125 °C |
| <b>Residual noise level in RMS spectral frequency range <math>\pm</math></b> | 1.5 mg        |
| <b>Maximum operational level (peak)</b>                                      | 500 g         |
| <b>Maximum shock level (<math>\pm</math> peak)</b>                           | 10000 g       |
| <b>Weight</b>  | 2.9 gram      |
| <b>Output</b>  | CCLD          |
| <b>Unigain</b>   | No            |
| <b>Triaxial</b>  | No            |
| <b>Resonance Frequency</b>   | 52 kHz        |

**Appendix C****Table 9: Summary of test operating conditions.**

| <b>Operating Condition</b>   | <b>Setting</b> |
|------------------------------|----------------|
| <b>VFD carrier frequency</b> | 2 kHz          |
| <b>Nominal input speed</b>   | 4 Hz           |
| <b>Nominal torque load</b>   | 50 Nm or 65 Nm |
| <b>Sampling frequency</b>    | 25.6 kHz       |
| <b>Sample length</b>         | 300 seconds    |

## Appendix D

### D.1 Code used to plot the example undamaged gear signal

```
% This program generates a number of time domain and frequency
plots
% for a single data sample

clear all
close all

load('041115_NoDamage_65Nm.mat')

% Set up time and frequency
N=length(Track3);
fs=N/RecordLength;
dt=1/fs;
t=(0:N-1)*dt;
f=(0:N-1)*fs/N;

%% Internal

% Plot time domain with tachometer signal
x=Track1;
plot_raw_time
title('Internal: Time Domain')

% Plot restricted time
x=Track1;
plot_raw_time
xlim([149 150])
title('Internal: Time Domain Segment')

% Plot log frequency
plot_raw_log_frequency
title('Internal: Frequency Spectrum')

% Plot restricted log frequency
plot_raw_log_frequency
xlim([0 25])
title('Internal: Frequency Spectrum Segment')

%% External

% Plot time domain with tachometer signal
x=Track2;
plot_raw_time
title('External: Time Domain')

% Plot restricted time
```

```
x=Track2;
plot_raw_time
xlim([149 150])
title('External: Time Domain Segment')

% Plot log frequency
plot_raw_log_frequency
title('External: Frequency Spectrum')

% Plot restricted log frequency
plot_raw_log_frequency
xlim([0 25])
title('External: Frequency Spectrum Segment')
```

**D.2 Time domain plotter**

```
% THIS PROGRAM PLOTS TIME DOMAIN FOR RAW DATA

% DECLARE x=Track1 or x=Track2 BEFORE RUNNING
% DECLARE fs BEFORE RUNNING

% Set up time and frequency
N=length(x);
dt=1/fs;
t=(0:N-1)*dt;
f=(0:N-1)*fs/N;

% Plot time domain with tachometer signal
figure
plot(t,x)
xlabel('Time (s)')
ylabel('Acceleration (m/s^2)')

% SET TITLE AFTER RUNNING
```

**D.3 Logarithmic frequency spectrum plotter**

```
% THIS PROGRAM PLOTS LOGARITHMIC FREQUENCY SPECTRUM FOR RAW DATA

% DECLARE x=Track1 or x=Track2 BEFORE RUNNING
% DECLARE fs BEFORE RUNNING

% Set up time and frequency
N=length(x);
dt=1/fs;
t=(0:N-1)*dt;
f=(0:N-1)*fs/N;

% Generate up the frequency spectrum and plot
X=abs(fft(x));
figure
semilogy(f,X)
xlabel('Frequency (Hz)')
ylabel('Amplitude (dB)')
xlim([0 max(f(1:N/2+1))])

% SET TITLE AFTER RUNNING
```



**D.4 Frequency difference in faulty signal plotter**

```

% This code plots time domain for a faulty signal
% and the frequency difference between faulty and non-faulty
signals

close all
clear all

load('041115_NoDamage_65Nm.mat')

% Set up time and frequency
N=length(Track3);
fs=N/RecordLength;
dt=1/fs;
t=(0:N-1)*dt;
f=(0:N-1)*fs/N;

a=Track1;
b=Track2;

A=(fft(a));
B=(fft(b));

% Set up faulty signal
load('041115_HalfRootCrack_65Nm.mat')

x=Track1;
plot_raw_time
xlim([149 150])
title('Internal: Time Domain Segment')

x=Track2;
plot_raw_time
xlim([149 150])
title('External: Time Domain Segment')

x=Track1;
y=Track2;

X=(fft(x));
Y=(fft(y));

% Plot frequency difference
figure
plot(f,abs(X-A))
xlabel('Frequency (Hz)')
ylabel('Amplitude (dB)')
title('Internal: Frequency Spectrum Difference')
xlim([0 max(f(1:N/2+1))])

```

```
figure
plot(f,abs(Y-B))
xlabel('Frequency (Hz)')
ylabel('Amplitude (dB)')
title('External: Frequency Spectrum Difference')
xlim([0 max(f(1:N/2+1))])
```

**D.5 Frequency spectrum comparison plotter**

```

% This code plots time domain for a faulty signal
% and the frequency comparison for faulty and non-faulty
signals

close all
clear all

load('041115_Spall_65Nm.mat')

% Set up time and frequency
N=length(Track3);
fs=N/RecordLength;
dt=1/fs;
t=(0:N-1)*dt;
f=(0:N-1)*fs/N;

a=Track1;
b=Track2;

A=(fft(a));
B=(fft(b));

% Set up faulty signal
load('041115_QuarterRootCrack_65Nm.mat')

x=Track1;
plot_raw_time
xlim([148 150])
title('Internal: Time Domain Segment')

x=Track2;
plot_raw_time
xlim([148 150])
title('External: Time Domain Segment')

x=Track1;
y=Track2;

X=(fft(x));
Y=(fft(y));

% Plot frequency comparison
figure
plot(f,abs(A),f,abs(X))
xlabel('Frequency (Hz)')
ylabel('Amplitude (dB)')
legend('Baseline' 'Spall')
title('Internal: Frequency Spectrum Comparison')
xlim([0 500])

```

```
figure
plot(f,abs(B), f,abs(Y))
xlabel('Frequency (Hz)')
ylabel('Amplitude (dB)')
legend('Baseline' 'Spall')
title('External: Frequency Spectrum Comparison')
xlim([0 500])
```

**D.6 Smoothing code**

```

close all
clear all
load('data.mat')

x=data5;

% Set up time and frequency
N=length(x);
dt=1/fs;
t=(0:N-1)*dt;
f=(0:N-1)*fs/N;

X=(1/N)*fft(x);

% Find dropouts
j=1;
drop=0.675;

for i=2:N-1
    diff=x(i-1)-x(i);
    diff2=x(i+1)-x(i);
    boolArray(i)=0;
    if (diff>drop)&(diff2>drop)
        boolArray(i)=1;
        diffIndex(j)=i;
        j=j+1;
    end
end
boolArray(N)=0;

num_dropouts=length(diffIndex)

% Plot dropouts frequency spectrum
A=fft(boolArray);
B=abs(A);

figure
plot(B)
xlabel('Frequency (Hz)')
ylabel('Magnitude')
title('Dropouts: Frequency Spectrum')
xlim([0 20000])

```

**D.7 Order tracking code**

```

function
[RsmPVib_P,RsmPGrid_P,Pulse,SmpPerRev,M_P,R,Nperiod,fr1,fr2]=O
rderTrack_Planet_Old(tac,vib, ratio,Vthold,SmpPerRev,Opt,dt)
%
%
[RsmPVib,RsmPGrid,Pulse]=OrderTrack(tac,vib, ratio,Vthold,SmpPe
rRev,Opt)
% This program uses the tacho signals to track the vibration
% data according to a ratio of the tacho pulses. There is a
small
% portion of the program that is taken from David Forrester's
% program.
%
% tac - Tacho signal
% vib - Vibration signal
% ratio - Ratio of ; Tacho pulse frequency to frequency of shaft
to be tracked
% Vthold - Threshold for triggering the tacho (--> triggering
times are in Pulse)
% TotSmp - Total number of samples in the vibration signal
% SmpPerRev - The desired number of samples per tracked
revolution
% Opt - (1) Find the exact sample number where the tacho goes
above the Vthold
% (2) Find the exact sample number where the tacho reaches its
max above the Vthold
% RsmPVib - Tracked signal
% RsmPGrid - New time grid
% NperiodNew - number of periods in averaging process
%
% -----
% Author : Dominique Ho
% Revised : J.Antoni 07/2001
% Revised : N.Sawalhi 03/2004 (calculate a residual signal (R))
% Revised: Wade Smith 10/2012 (outputs number of periods in
averaging
% process, calculates shaft speed, determines samples per
revolution
% automatically by calling SamplesPerRev function)
% -----
vib=vib(:)';
tac=tac(:)';
UndVth=find(tac<=Vthold); %Find all samples under Vthold
I = find(diff(UndVth)>1);
SmpUndVth=UndVth(I); %Find samples under Vthold at start of
pulse
if nargin < 6 || Opt == 1
    % Find the exact sample number where the tacho goes above
the Vthold

```

```

    Pulse=SmpUndVth+(Vthold-
tac(SmpUndVth))./(tac(SmpUndVth+1)-tac(SmpUndVth));
else
    if min(tac)<0,disp('Caution : The tacho signal should be >=
0 !!');end
    if I(end)==length(UndVth),I(end)=I(end)-1;end
    SmpUndVth2=UndVth(I+1); %Find samples under Vthold at end
of pulse
    % Find the exact sample number where the tacho reaches its
max above the Vthold
    K = length(I);Pulse=zeros(1,K);
    for k=1:K

Pulse(k)=sum((SmpUndVth(k):SmpUndVth2(k)).*(tac(SmpUndVth(k):S
mpUndVth2(k))));

Pulse(k)=Pulse(k)/sum(tac(SmpUndVth(k):SmpUndVth2(k)));
    end
end
Kp = length(Pulse); KT = Kp;
%% This part added by Wade Smith to determine average shaft
speed - 23 Oct 2012
diff_pulse=Pulse(end)-Pulse(1); %difference in pulse no between
last pulse and first pulse
ave_diff_pulse=diff_pulse/(length(Pulse)-1); %average
difference
% Obtain shaft period (above difference converted to time
units):
shaft_period=ave_diff_pulse*dt;
% Speed of ref shaft (Hz):
fr1=1/shaft_period;
fr2=fr1;
%% Find exact number of periods with a gear ratio different than
1, and
% calculate speed of tracked shaft;
if ratio ~= 1
    KT = fix((Kp-1)/ratio);
    fr2=fr1/ratio;
end
Nperiod=KT;
TotSmp=length(vib);
%% If SmpPerRev=0, SmpPerRev is calculated automatically
if SmpPerRev==0
    l_pulse=Pulse(end)-Pulse(1);
    % [SmpPerRevNew]=SamplesPerRev(l_pulse/Nperiod); %call
SamplesPerRev function
    % SmpPerRev=SmpPerRevNew;
    SmpPerRev=fix(l_pulse/Nperiod);
end
%% Ensure number of periods is divisible by 2 or 5:

```

```

if (rem(Nperiod,2) ~= 0) && (rem(Nperiod,5) ~= 0) % must be
divisible by 2 or 5
    NperiodNew=Nperiod-1;
else
    NperiodNew=Nperiod;
end
Nperiod=NperiodNew;
RsmvVib_P=[];
RsmvGrid_P=[];
RsmvGrid_P
interpl(1:Kp,Pulse,linspace(1, ratio*Nperiod+1, SmpPerRev*Nperio
d+1), '*pchip');
RsmvVib_P = interpl((1:TotSmp), vib, RsmvGrid_P, '*pchip');
RsmvVib_P = RsmvVib_P(1:SmpPerRev*Nperiod);
% Evaluating the Synchronous average (M) &
% R ( Signal minus average)
M_P = mean(RsmvVib_P);
R = RsmvVib_P - M_P;

```



**D.8 Code to plot order-tracked samples**

```
clear all;
close all;

%load('041115_HalfRootCrack_65Nm.mat');
load('041115_NoDamage_65Nm.mat');
vib = Track1;
tac = Track3;

Vthold=max(Track3)/2;
N=length(Track3);
fs=N/RecordLength;
dt=1/fs;
ratio = 1/1.89;
SmpPerRev = 0;
Opt = 1;

[RsmpVib_P,RsmpGrid_P,Pulse,SmpPerRev,M_P,R,Nperiod,fr1,fr2] =
OrderTrack_Planet_New(tac,vib,ratio,Vthold,SmpPerRev,Opt,dt);

endTime = N/fs;
revEnd = fr2*endTime;

dataSet = R;

rlen = length(dataSet);

dRev = linspace(0,revEnd,rlen);

plot(dRev,dataSet);
xlabel('Revolutions');
ylabel('Acceleration (m/s^2)');
title('Order Tracked Data')
axis tight;

truncVib = dataSet;

RFFT = fft(truncVib)/rlen;

x = truncVib;

% Set up time and frequency
N=length(x);
dt=1/fs;
t=(0:N-1)*dt;
f=(0:N-1)*fs/N;

% Plot spectrum
X=fft(x)/N;
figure
```

```
RLog = 10*log10(abs(RFFT)/(10^(-6)));  
plot(f(1:N/2+1)/fr2, abs(X(1:N/2+1)))  
% plot(f/fr2, RLog)  
xlabel('Orders')  
ylabel('Magnitude')  
xlim([0 100])  
title('Order Tracked Data')
```